The Pennsylvania State University

The Graduate School

Department of Electrical Engineering

COMPARISON OF THREE-PHASE CURRENT CONTROLLERS FOR PERMANENT MAGNET SYNCHRONOUS MACHINE DRIVES

A Thesis in

Electrical Engineering

by

Shuo Chen

Submitted in Partial Fulfillment
of the Requirements
for the Degree of
Master of Science

August 2014

The thesis of Shuo Chen was reviewed and approved* by the following:

Jeffrey Mayer
Associate Professor of Electrical Engineering
Thesis Advisor

Jeffrey Schiano
Associate Professor of Electrical Engineering

Kultegin Aydin
Professor of Electrical Engineering
Department Head

*Signatures are on file in the Graduate School

ABSTRACT

Field-oriented control (FOC) is a defacto standard for the high-performance control of inverter-driven ac electric machines. FOC requires regulation of the three-phase ac stator winding currents within a velocity/position control loop. It is usually accomplished using PI control in the synchronous reference frame in conjunction with appropriate reference frame transformations for the current feedback signals and voltage actuation signals.

In this thesis, transfer function models have been derived for a complete drive system with FOC, and are used to compare the characteristic response of the various approaches. Among these transfer functions, the use of the synchronous reference frame starts from practical considerations. In particular, all the electrical variables in this frame are dc quantities in the steady state; thus, compensator bandwidth is ostensibly a minor concern. Analysis of the closed-loop system, however, reveals a potential hidden cost in this approach: it imposes a bandwidth limitation on the velocity/position control loop.

A set of Simulink models for drive system components has also been developed to investigate the large signed, non-linear response of these systems with different controllers. The Simulink models also permit selective modeling of non-idealities such as blanking time.

TABLE OF CONTENTS

LIST OF FIGURES

LIST OF TABLES

ACKNOWLEDGEMENTS

I would like to thank my advisor, Jeffrey S.Mayer, for providing me with his support, guidance, and priceless advice.

Chapter 1

Introduction

1.1 Motivation

Permanent magnet synchronous machine (PMSM) drives are widely used in industrial applications, ranging from general purpose pump and conveyor drives to high-performance machine tool and robotic drives. They are also the most common type of drive used in electric and hybrid electric vehicles. Among the attributes that make PMSM drives attractive in these applications are a high torque density, a high efficiency, and a high degree of controllability. The first two attributes stem from the construction of the PMSM using high-energy permanent magnets to produce the rotor magnetic flux. The last attribute stems from the use of a three-phase inverter (dc-to-ac converter) for driving the stator windings of the machine and the use of resolvers or encoders for rotor position feedback.

Various control schemes are possible for PMSM drive systems. The two most common are referred to as Brushless DC Motor (BDCM) control and Field-Oriented Control (FOC). BDCM control, also referred to as Electronically Commutated Motor (ECM) control, was the first scheme, and it is the simplest. It involves switching the respective phases of the inverter based solely on the rotor position – hence there is a similarity to the mechanical commutation process in conventional dc machines but without an actual commutator and brushes. The price for the simplicity of BDCM mode is that the torque angle between the rotor permanent magnet flux and the stator winding flux is not fixed, so the torque developed by the machine cannot be controlled directly, as the torque involves the product of the sine of the torque angle and the magnitude of

the stator winding flux. The magnitude of the stator winding flux can be controlled, if the magnitude of the phase voltages provided by the inverter can be varied, as through pulse width modulation (PWM) of the inverter switching. Such control of the magnitude of the stator flux but not its angle is sometimes referred to as scalar control in contradistinction to vector control or FOC, in which both the magnitude and angle of the stator flux are controlled [1][2][3].

For FOC, which is the control scheme used in high-performance applications, the overall drive system controller is implemented using a nested loop structure in which the outer loop is for velocity control, and the inner loop is for three-phase current control. From the standpoint of the velocity controller, the inverter-PMSM combination is treated as a nearly ideal torque source, with the velocity controller providing a reference torque that is merely scaled and augmented with a zero to produce a reference current vector for the inner current control loop. The three-phase current controller is more complicated, because one or more reference frame transformations must be used in order to calculate useful error and actuation signals. More specifically, the reference current vector is constant in the steady state while the components of the feedback current vector vary sinusoidally at a frequency corresponding to the rotor velocity.

Early in the development of FOC systems (circa 1990), microcontroller clock speed limitations led to the selection of so-called synchronous reference frame proportional plus integral (PI) control, in which the feedback current vector was transformed into the synchronous reference frame wherein the vector is constant in the steady state. With this reference frame transformation performed by an application specific integrated circuit (ASIC), only PI control involving low-frequency signals needed to be implemented on the microcontroller, while an inverse transformation and sinusoidal PWM required for the actuation signals to the inverter were handled by another ASIC. As microcontroller capabilities increased, the reference frame transformations and PWM functions were brought into the microcontroller. Thus, the synchronous reference frame PI control scheme came to be used widely.

As the performance objectives for drive systems increased, the frequency of the variables associated with the synchronous reference frame PI controller also increased. This did not pose a significant problem with respect to the microcontroller, because microcontroller capabilities increased concurrently. Eventually, however, it was observed that the current control loop had an upper frequency or bandwidth limit not related to hardware but to the control scheme itself [4]. A stationary reference frame proportional control scheme was suggested as an alternative.

The purpose of this thesis is to analyze the bandwidth limitation of several current control schemes and the impact of such limitations on the performance of the velocity control loop in PMSM drive systems. Particular attention is given to stationary reference frame proportional control and to synchronous reference PI control.

1.2 Contribution

This thesis provides a comparison of several three-phase current control schemes used in permanent magnet synchronous machine drive systems. The comparison is made through derivation and analysis of closed-loop transfer functions and through simulation in Simulink. Current control in a three-phase RL circuit is considered initially. The impact of the current control loop on the velocity control loop of the PMSM drive system is then considered.

A second contribution of this project is the creation of a simulation test bed to facilitate investigating the affect of non-idealities in PMSM drive systems. For example, time delays and dead time in the actuation signals to the inverter.

1.3 Organization

The thesis is organized in five chapters. Chapter 2 provides a brief overview of PMSM drive systems and mathematical models for the PMSM and three-phase inverter. Chapter 3 provides an analysis of three-phase current control in an RL circuit for several different control schemes, including stationary reference frame proportional control, and synchronous reference frame PI control with and without electrical motive force (EMF) compensation. Chapter 4 provides an analysis of the effect of the various three-current control schemes on the velocity control loop of the PMSM drive system. Chapter 5 concludes the thesis and provides recommendations for future work.

Chapter 2

Permanent Magnet Synchronous Machine Drive Systems

This chapter provides a description of a typical permanent magnet synchronous machine (PMSM) drive system and its key components. Such a system is a closed-loop system in which a digital controller is used for both velocity control (outer loop) and current control (inner loop). Historically, the implementation of the current control loop was a critical problem due to limitations imposed by the digital controller and power electronics hardware. Those limitations are described in this chapter. With present-day availability of faster controller and power hardware, the original limitations have become less important, so that it is now the control algorithm itself that imposes limitations. That is the topic of the next chapter.

2.1 PMSM Drive System

A typical PMSM drive system is comprised of three major components: the PMSM itself, an inverter, and a digital controller that may be a microcontroller or FPGA. The PMSM is connected to a mechanical system via a shaft. An encoder or resolver mounted on the shaft provides feedback of the PMSM rotor position and velocity. A top-level block diagram of the system is shown in Figure 2-1, wherein the nested control loop structure is evident.

The velocity control or outer loop is similar to that of a conventional dc machine drive system operated under current-mode control. In particular, a velocity error determined by subtracting the velocity feedback signal ω_r from a reference velocity ω_r^* is acted on by a

compensator or controller that produces a reference current signal $\mathbf{i}_{sdq}^{r*}$. In the case of the PMSM drive system, the reference current signal is a vector comprised of the so-called rotor reference frame d- and q-axis components of the three-phase ac stator current $\mathbf{i}_{sabc}$. Details about the rotor reference frame are provided in the next section on the PMSM and its mathematical model. For now, however, we note that the electromagnetic torque developed by a PMSM is proportional to the q-axis (2nd) component of $\mathbf{i}_{sdq}^{r*}$ and that under steady state conditions $\mathbf{i}_{sdq}^{r*}$ is constant, while $\mathbf{i}_{sabc}$ varies at a frequency corresponding to the rotor velocity ω_r – the rotor position feedback signal θ_r, which has rate ω_r, is used in one or more reference frame transformations to account for the frequency difference between $\mathbf{i}_{sdq}^{r*}$ and $\mathbf{i}_{sabc}$.

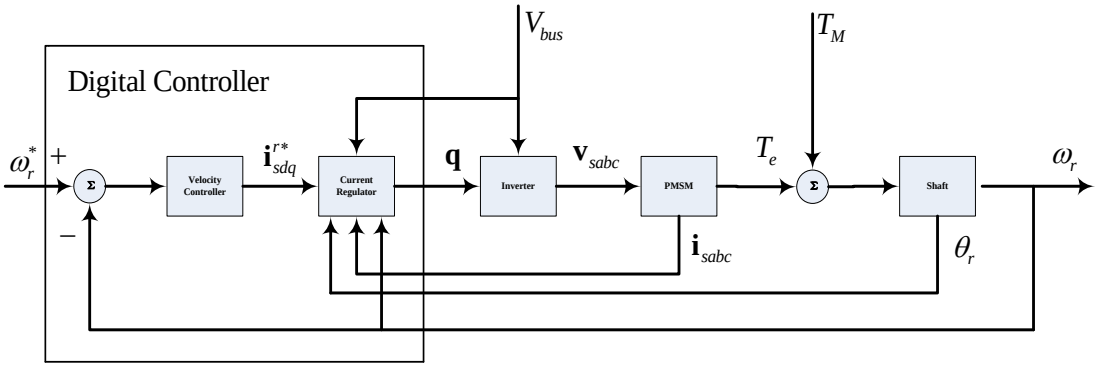

Figure 2-1. Top-level block diagram of a typical PMSM drive system.

The current controller can be implemented in a variety of ways [5]. In almost all of these, the output of the current controller is a vector of pulse width modulated (PWM) gating signals **q** that is sent to the three-phase inverter that is comprised of transistors operated as switches. The inverter synthesizes three-phase ac voltage $\mathbf{v}_{sabc}$ from a dc bus voltage V_{bus} based on the gating signals. Details about the inverter and its operation are presented in Section 2.3. For now, however, we note two important points. First, there is a control effort limit imposed by V_{bus}, as

the amplitude of the sinusoidal component of each entry of $\mathbf{v}_{sabc}$ at frequency ω_r can never exceed $V_{bus}/\sqrt{3}$. Second, there is bandwidth limit imposed by a combination of the maximum switching frequency of the transistors and the related pulse width modulation process.

Because the current loop bandwidth limit stems from the combination of a non-linear switching process in the inverter and a related discrete-time modulation process in the digital controller, it is not manifest as the familiar 20-dB or 40-dB roll-off in the frequency response of a continuous-time compensator. Instead, it is related to the minimum time necessary to perform the control algorithm calculations – the bandwidth limit is lower for a low microprocessor clock frequency and for a complicated control algorithm.

For early generation PMSM drives (circa. 1990), low microprocessor clock frequencies dictated implementation of the current controller in the rotor (or synchronous) reference frame wherein all variables of interest are dc in the steady state. Reference frame transformations and modulators associated with the ω_r -frequency variables were implemented in specialized analog or mixed-signal hardware. With the advent of faster microprocessors, all tasks could be moved into the microcontroller. But this is not necessarily the best solution. As discussed in the next chapter, synchronous reference frame PI control imposes a bandwidth limitation of its own. Implementing the current controller in the stationary reference frame wherein all variables of interest vary at frequency ω_r may make more sense.

2.2 Permanent Magnet Synchronous Machine

In this section, the PMSM is described in terms of its physical design and a mathematical model suitable for analyzing a PMSM drive system.

2.2.1 Structure and Types of Permanent Magnet Synchronous Machines

The PMSM is a rotating electric machine that includes a three-phase ac stator like that of an induction machine or conventional synchronous machine. The field flux is produced by permanent magnets that are bonded to the surface of the rotor or embedded within the rotor as shown in Figures 2-2 and 2-3, respectively. The former type is referred to as a surface mount permanent magnet (SMPM) synchronous machine, and the latter is referred to as an interior permanent magnet (IPM) synchronous machine. Modern high-energy permanent magnets produce a substantial air gap magnetic flux making it possible to construct machines with high power-to-weight ratios and efficiencies.

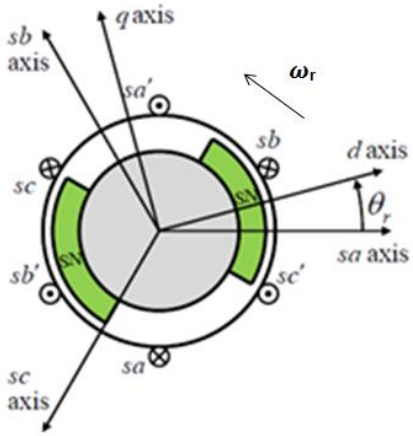

Figure 2-2. SMPM.

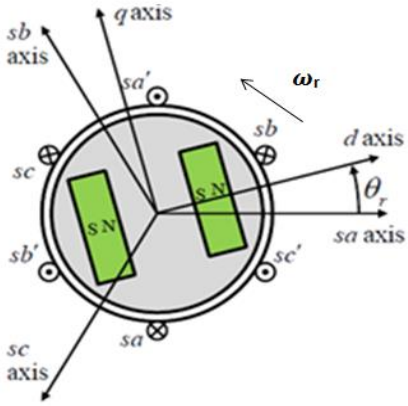

Figure 2-3. IPM.

The three-phase stator winding of a PMSM is driven by three-phase sine-wave voltages whose instantaneous phase is related to the rotor position θ_r ; thus, the frequency of the voltages corresponds to the rotor velocity ω_r . This imposed synchronization requires the use of a three-phase dc-to-ac inverter, key attributes of which are provided in the next section. The stator flux resulting from the applied stator winding voltages interacts with the field flux produced by the rotor permanent magnets to yield an electromagnetic torque that acts on the rotor. To obtain the best performance, the sine wave voltages should result in a stator flux that is 90 °ahead of the

rotor flux. Regulating the angle between the stator and rotor flux is achieved by controlling the three-phase stator winding currents, which are related to the stator voltages by Ohm's law and Faraday's law and to the stator flux by Ampere's law.

2.2.2 Mathematical Model

The mathematical model of the PMSM that is suitable for control system analysis is derived though application of first principles and reference frame theory. Key assumptions underlying the modeling process are:

- The machine can be represented by a lumped parameter model.
- The machine is a 2-pole machine. All results can be readily extended to a *P*-pole machine by scaling positions, velocities/frequencies, and torques by 2/*P* or *P*/2.
- The three-phase stator windings are sinusoidally distributed and displaced by 120° [14], as shown in Figure 2-4.
- The air-gap magnetic flux density produced by the rotor permanent magnets is sinusoidally distributed.
- The magnetic system is linear.

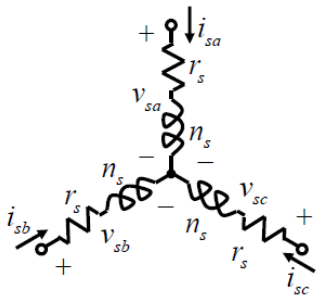

Figure 2-4. Schematic diagram of three-phase stator winding.

2.2.2.1 First Principles Model

Since the stator winding is a three-phase winding, there are three voltage equations based on Ohm's law and Faraday's law, and three flux linkage equations that can be written in terms of the three winding currents and the rotor permanent magnet flux. The matrix-vector forms of these equations are:

$$\mathbf{v}_{sabc} = \mathbf{r}_s \mathbf{i}_{sabc} + \frac{d}{dt}\boldsymbol{\lambda}_{sabc} \tag{2.1}$$

$$\boldsymbol{\lambda}_{sabc} = \mathbf{L}_s(\theta_r)\mathbf{i}_{sabc} + \boldsymbol{\lambda}'_{sm}(\theta_r) \tag{2.2}$$

where $\mathbf{v}_{sabc}$ is the three-phase stator voltage, $\mathbf{i}_{sabc}$ is the three-phase stator currents, and $\boldsymbol{\lambda}_{sabc}$ is the three-phase stator flux linkage:

$$\mathbf{v}_{sabc} = \begin{bmatrix} v_{sa} \\ v_{sb} \\ v_{sc} \end{bmatrix} \qquad \mathbf{i}_{sabc} = \begin{bmatrix} i_{sa} \\ i_{sb} \\ i_{sc} \end{bmatrix} \qquad \boldsymbol{\lambda}_{sabc} = \begin{bmatrix} \lambda_{sa} \\ \lambda_{sb} \\ \lambda_{sc} \end{bmatrix}$$

The part of the stator flux linkage due to the rotor permanent magnets is:

$$\boldsymbol{\lambda}'_{sm}(\theta_r) = \lambda'_{sm}\begin{bmatrix} \cos(\theta_r) \\ \cos(\theta_r - \frac{2\pi}{3}) \\ \cos(\theta_r + \frac{2\pi}{3}) \end{bmatrix} \tag{2.3}$$

where λ'_{sm} accounts for the number of turns of the stator winding and the flux density of the rotor permanent magnets.

The parameter matrices in (2.1) and (2.2) are:

$$\mathbf{r}_s = \begin{bmatrix} r_s & 0 & 0 \\ 0 & r_s & 0 \\ 0 & 0 & r_s \end{bmatrix} = r_s \mathbf{I}, \tag{2.4}$$

$$\mathbf{L}_s(\theta_r) = \begin{bmatrix} L_{ls} + L_A + L_B\cos(2\theta_r) & -\frac{1}{2}L_A + L_B\cos(2\theta_r - \frac{2\pi}{3}) & -\frac{1}{2}L_A + L_B\cos(2\theta_r + \frac{2\pi}{3}) \\ -\frac{1}{2}L_A + L_B\cos(2\theta_r - \frac{2\pi}{3}) & L_{ls} + L_A + L_B\cos(2\theta_r + \frac{2\pi}{3}) & -\frac{1}{2}L_A + L_B\cos(2\theta_r) \\ -\frac{1}{2}L_A + L_B\cos(2\theta_r + \frac{2\pi}{3}) & -\frac{1}{2}L_A + L_B\cos(2\theta_r) & L_{ls} + L_A + L_B\cos(2\theta_r - \frac{2\pi}{3}) \end{bmatrix} \tag{2.5}$$

where the L_A and L_B are related to the d- and q-axis magnetizing inductances L_{md} and L_{mq} by

$$\begin{aligned} L_A &= \tfrac{1}{3}(L_{md} + L_{mq}) \\ L_B &= \tfrac{1}{3}(L_{md} - L_{mq}) \end{aligned} \tag{2.6}$$

The electromagnetic torque can be expressed by taking the partial derivative of co-energy with respect to θ_r:

$$\begin{aligned} T_e &= \frac{\partial W_c(\mathbf{i}_{sabc}, \theta_r)}{\partial \theta_r} \\ &= \tfrac{1}{2}\mathbf{i}_{sabc}^T \left(\frac{\partial}{\partial \theta_r}\mathbf{L}_s(\theta_r) \right)\mathbf{i}_{sabc} + \mathbf{i}_{sabc}^T \frac{\partial}{\partial \theta_r}\boldsymbol{\lambda}'_{sm}(\theta_r) \end{aligned} \tag{2.7}$$

An equation of motion for the mechanical system can be expressed by applying Newton's second law for rotational systems to the (actual) mechanical system:

$$J\frac{d}{dt}\omega_{r(\text{shaft})} = T_{e(\text{shaft})} - T_M - D\omega_{r(\text{shaft})} \tag{2.8}$$

where

$$\omega_{r(\text{shaft})} = \frac{2}{P}\omega_r \tag{2.9}$$

$$T_{e(\text{shaft})} = \frac{P}{2}T_e \tag{2.10}$$

The parameters J and D in (2.8) are the combined rotational inertias of the machine and load in $\text{kg} \cdot \text{m}^2$ and a linear drag coefficient in N·m·s/rad. The parameter *P* is the number of poles.

2.2.2.2 Rotor Reference Frame Transformation

The preceding first-principles model is not very practical for relating electrical and mechanical port variables due to the position-dependent mutual inductances in the flux linkage

equation (2.2) and the torque equation (2.7). To facilitate analysis, the rotor reference frame transformation of the stator variables is used to eliminate the position-dependent mutual inductances. This transformation is expressed as

$$\mathbf{f}^{r}_{sdq0} = \mathbf{T}(\theta_r)\mathbf{f}_{sabc} \tag{2.11}$$

where **f** may represent **v**, **i**, or **λ** and

$$\mathbf{f}^{r}_{sdq0} = \begin{bmatrix} f^{r}_{sd} \\ f^{r}_{sq} \\ f^{r}_{s0} \end{bmatrix} \tag{2.12}$$

$$\mathbf{T}(\theta_r) = \tfrac{2}{3}\begin{bmatrix} \cos(\theta_r) & \cos(\theta_r - \frac{2\pi}{3}) & \cos(\theta_r + \frac{2\pi}{3}) \\ -\sin(\theta_r) & -\sin(\theta_r - \frac{2\pi}{3}) & -\sin(\theta_r + \frac{2\pi}{3}) \\ \frac{1}{2} & \frac{1}{2} & \frac{1}{2} \end{bmatrix} \tag{2.13}$$

After transformation, (2.1), (2.2), and (2.7) become:

$$\mathbf{v}^{r}_{sdq0} = \mathbf{r}_s\mathbf{i}^{r}_{sdq0} + \omega_r\mathbf{J}\boldsymbol{\lambda}^{r}_{sdq0} + \frac{d}{dt}\boldsymbol{\lambda}^{r}_{sdq0} \tag{2.14}$$

$$\boldsymbol{\lambda}^{r}_{sdq0} = \mathbf{L}^{r}_{s}\mathbf{i}^{r}_{sdq0} + \boldsymbol{\lambda}'^{r}_{sm} \tag{2.15}$$

$$T_e = \frac{3}{2}\lambda'_{sm}i^{r}_{sq} + \frac{3}{2}(L_{md} - L_{mq})i^{r}_{sq}i^{r}_{sd} \tag{2.16}$$

where

$$\mathbf{J} = \begin{bmatrix} 0 & -1 & 0 \\ 1 & 0 & 0 \\ 0 & 0 & 0 \end{bmatrix} \tag{2.17}$$

$$\mathbf{L}^{r}_{s} = \begin{bmatrix} L_d & 0 & 0 \\ 0 & L_q & 0 \\ 0 & 0 & L_{ls} \end{bmatrix} \tag{2.18}$$

$$\begin{aligned} L_d &= L_{ls} + L_{md} \\ L_q &= L_{ls} + L_{mq} \end{aligned} \tag{2.19}$$

$$\boldsymbol{\lambda}'^{r}_{sm} = \begin{bmatrix} \lambda'_{sm} \\ 0 \\ 0 \end{bmatrix} \tag{2.20}$$

The stator windings are usually connected in an un-grounded wye or delta, so the zero-sequence components for all variables can be ignored.

From equation (2.13), we see that the electromagnetic torque is simply proportional to i^r_{sq} if i^r_{sd} is zero. Thus, the current reference signal is usually of the form

$$\mathbf{i}^{r*}_{sdq} = \begin{bmatrix} 0 \\ i^{r*}_{sq} \end{bmatrix} \tag{2.21}$$

2.2.2.3 Per-Unit Model

The per-unit system is a method of expressing quantities in an electrical system (e.g. voltage, current, impedance, etc.) as a proportion of pre-defined base quantities. By definition, the per-unit value of a quantity is the ratio of the original quantity to its base value (which results in a dimensionless "per-unit" or "pu" value):

$$Q_{pu} = \frac{Q}{Q_{base}}$$

where Q_{pu} is the per-unit quantity (dimensionless or just "pu")

Q is quantity in normal units

Q_{base} is the base value of the quantity in normal units [14]

By using per-unit value calculations especially manual one could be simplified: 1) Kilo or Mega will not show up any more (as long as base value is high enough); 2) confusion between qualities (line-line, line-neutral) could be eliminated, 3) per-unit impedances of transformers are

the same whether referred to either side of the transformer (primary or secondary) and are independent of winding connections (for poly-phase transformers), voltage level and phase shifts.

Before using the per-unit model, the following units are first defined below: angular frequency, torque, power, voltage, impedance and current:

$$\omega_{base} = \frac{P}{2}\frac{2\pi}{60} n_{rated} \qquad \text{(Angular frequency base)}$$

$$T_{base} = T_{rated} = \frac{P}{2}\frac{S_{base}}{\omega_{base}} \qquad \text{(Torque base)}$$

$$S_{base} = P_{base} = P_{rated} = \frac{2\pi}{60} n_{rated} T_{rated} \qquad \text{(Power base)}$$

$$V_{base(abc)} = \frac{1}{\sqrt{3}} V_{rated} \qquad V_{base(dq)} = \frac{\sqrt{2}}{\sqrt{3}} V_{rated} \qquad \text{(Voltage base)}$$

$$Z_{base} = \frac{V_{rated}^2}{S_{base}} \qquad \text{(Impedance base)}$$

$$I_{base(abc)} = \frac{1}{3}\frac{S_{base}}{V_{base(abc)}} \qquad I_{base(dq)} = \frac{2}{3}\frac{S_{base}}{V_{base(dq)}} \qquad \text{(Current base)}$$

Equation (2.14) – (2.16) become (2.22) – (2.24) after dividing by the appropriate bases:

$$\mathbf{v}_{sdq0}^{r} = \mathbf{r}_s \mathbf{i}_{sdq0}^{r} + \omega_{r(\text{pu})} \mathbf{J} \boldsymbol{\psi}_{sdq0}^{r} + \frac{1}{\omega_{base}} \frac{d}{dt} \boldsymbol{\psi}_{sdq0}^{r} \qquad (2.22)$$

$$\boldsymbol{\psi}_{sdq0}^{r} = \mathbf{X}_s^{r} \mathbf{i}_{sdq0}^{r} + \boldsymbol{\psi}_{sm}^{\prime r} \qquad (2.23)$$

$$T_e = \psi_{sm}^{\prime r} i_{sq}^{r} + (X_{md} - X_{mq}) i_{sq}^{r} i_{sd}^{r} \quad \text{(pu)} \qquad (2.24)$$

$$2H \frac{d}{dt} \omega_{r(pu)} = T_M - T_e - D\omega_{r(pu)} \quad \text{(pu)} \qquad (2.25)$$

where $$H = \frac{1}{2}\frac{\frac{2}{P}\omega_{base}}{T_{base}} J \qquad D_{(pu)} = \frac{2}{P}\omega_{base} D$$

2.2.2.4 State Space Model

A non-linear state space model for the PMSM drive system can be expressed by manipulating (2.22) and (2.25) and including an auxiliary equation to relate $\mathbf{i}^r_{sdq}$ to $\boldsymbol{\psi}^r_{sdq}$. The Simulink model is shown in Appendix A.

$$\frac{d}{dt}\boldsymbol{\psi}^r_{sdq} = \omega_{base}\left(\mathbf{v}^r_{sdq} - \mathbf{r}_s\mathbf{i}^r_{sdq} - \omega_{r(pu)}\mathbf{J}\boldsymbol{\psi}^r_{sdq}\right) \tag{2.26}$$

$$\frac{d}{dt}\omega_{r(pu)} = \frac{1}{2H}\left(T_M - T_e - D\omega_{r(pu)}\right) \quad \text{(pu)} \tag{2.27}$$

$$\frac{d}{dt}\theta_r = \omega_{r(pu)} \tag{2.28}$$

$$\mathbf{i}^r_{sdq} = \mathbf{X}_s^{-1}(\boldsymbol{\psi}^r_{sdq} - \boldsymbol{\psi}'^r_{sm}) \tag{2.29}$$

2.2.3 Parameters of PMSM

The PMSM parameters used in this thesis are chosen from p. 271 of [6], which is shown in Table 2-1:

Table 2-1. PMSM parameter values used throughout this thesis.

$J = 10^{-4}\,\text{kg?m}^2$	$D = 10^{-5}\,\text{N}\cdot\text{m}\cdot\text{s/rad}$	$P = 4$	$A = 1$
$r_s = 1.5\Omega$	$L_d = 6.5\times10^{-3}\,\text{H}$	$L_q = 6.5\times10^{-3}\,\text{H}$	$\lambda^r_{sm} = 8.6603$

2.3 Inverter

An inverter is a switch-mode power converter that converts direct current (dc) to alternating current (ac). For applications involving less than approximately 1 kW, power

MOSFETs are frequently used as the switching devices. For the more numerous applications involving more than 1 kW, IGBTs (insulated gate bipolar transistors) are used. Switching losses in the IGBT typically limit the switching frequency that may be used to the order of 10 kHz.

Switching is inherently a non-linear process and introduces harmonics of the output frequency. The harmonic spectrum depends on the form of switching or pulse width modulation.

2.3.1 Single-phase Half-bridge VSI

Single-phase half-bridge VSI is also known as "inverter leg", which is basic building block for full-bridge, three phase and higher order inverters. Two capacitors in the circuit share the same value, divide the dc voltage as $\frac{1}{2}V_{dc}$. Two switches in the circuit (S_1 and S_2 in figure below) normally are IGBT, which could be controlled by PWM signal at gate. Since these two switches are complementary to each other, voltage over load could be either $\frac{1}{2}V_{dc}$ or $-\frac{1}{2}V_{dc}$. The composition and output voltage of single-phase half-bridge VSI are shown below in Figure 2-5.

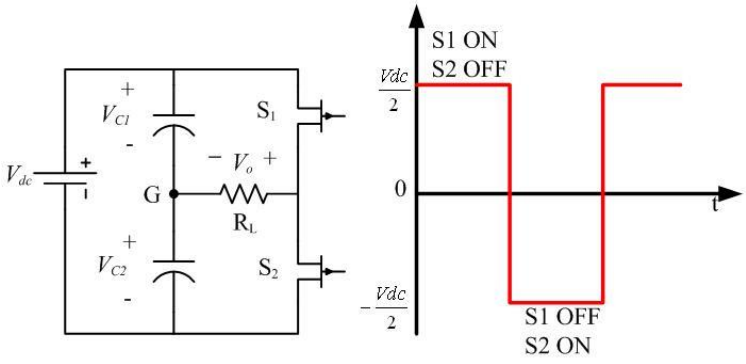

Figure 2-5. Schematic diagram and output voltage of single-phase half-bridge VSI.

2.3.2 Three-phase Full-bridge VSI

The three-phase full-bridge VSI can be considered as the combination of three single-phase VSI as shown in Figure 2-6. For switches in the same leg, S1 and S4 for example, they must be complement to each other (if not consider blank time). Also, three legs are delayed by 120° to each other to generate three-phase supply.

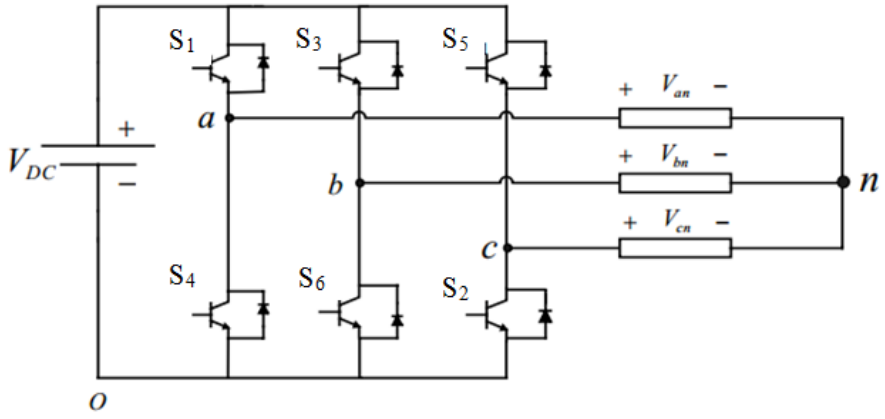

Figure 2-6. Schematic diagram of three-phase full-bridge voltage source inverter.

Compared to square wave switching, sinusoidal pulse width modulation (SPWM) is widely used in power electronics to digitize the power so that a sequence of voltage pulses can be generated by the on and off of the power switches. SPWM techniques are characterized by constant amplitude pulses with different duty cycles for each period. The width of these pulses are modulated to obtain inverter output voltage control and to reduce its harmonic content [7]. Sinusoidal pulse width modulation is the mostly used method in motor control and inverter application [16]. In SPWM technique three sine waves and a high frequency triangular carrier wave are used to generate PWM signal [8].

Digital implementation SPWM technique is based on classical SPWM technique with carriers and reference sine waveform. Only difference between them is, in digital SPWM a sine table consisting of values of sine waveform sampled at certain frequency is used. As a result reference wave form in digital SPWM represents a sample and hold waveform of sine wave

forms. This sampling of sine waveform comes in two variants; a) Symmetrical sampling, b) Asymmetrical sampling. In both ways a delay would be introduced in output waveform. When the ratio of switch frequency to reference frequency is small, this delay would be significant, causing a frequency response roll-off which obeys a Bessel function [9]. Considering this, carrier wave must be in a high frequency. However, due to physical structure of modulator, there exists a bandwidth limitation. Considering this, reference wave must be in a low frequency, which brings synchronous reference frame that can eliminate bandwidth limitation into life.

Chapter 3

Current Control for Three-Phase RL Circuit

For permanent magnet synchronous machines (PMSM), torque is proportional to the magnitude of the q-axis component of the current vector and to the sine of the rotor angle as long as the d-axis component of the current vector is zero. The bandwidth of the current loop is important because the outer velocity-loop or position-loop dependents on it. In this chapter, we analyze the origin of the bandwidth limitation in inner current-loop that arises with different control schemes. For simplicity, we focus on a three-phase RL circuit to represent the stator winding of the PMSM in this chapter. The rotor permanent magnets and the rest of the PMSM are considered in the next chapter.

3.1 Introduction

A mechanical diagram and stator winding diagram for a generic round-rotor ac machine are shown in Figure 3-1. The stator winding will be treated simply as a three-phase RL circuit in this chapter.

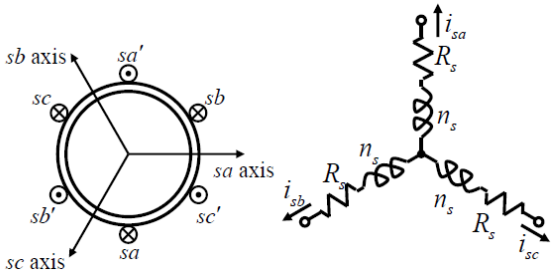

Figure 3-1. Mechanical diagram and winding diagram for the stator of a three-phase ac machine.

The relevant voltage equations of the RL circuit can be expressed as:

$$\begin{bmatrix} v_{sa} \\ v_{sb} \\ v_{sc} \end{bmatrix} = \begin{bmatrix} R_s & 0 & 0 \\ 0 & R_s & 0 \\ 0 & 0 & R_s \end{bmatrix} \begin{bmatrix} i_{sa} \\ i_{sb} \\ i_{sc} \end{bmatrix} + \begin{bmatrix} L_{ls}+L_{ms} & -\frac{1}{2}L_{ms} & -\frac{1}{2}L_{ms} \\ -\frac{1}{2}L_{ms} & L_{ls}+L_{ms} & -\frac{1}{2}L_{ms} \\ -\frac{1}{2}L_{ms} & -\frac{1}{2}L_{ms} & L_{ls}+L_{ms} \end{bmatrix} \frac{d}{dt} \begin{bmatrix} i_{sa} \\ i_{sb} \\ i_{sc} \end{bmatrix} \tag{3.1}$$

Depending on the reference frame in which a current controller acts, the current control schemes for a permanent magnet synchronous machine (PMSM) drive can be classified into two categories, namely, stationary frame control or synchronous frame control[10]. The first one relies on Clarke's transformation, which is can be expressed using a constant matrix, so the frequency of the transform variables is the same as the frequency of the phase variables [11]. The second one relies on Park's transformation, which depends on the rotor position θ_r, so the frequency of the transform variables is dc in the steady state [12]. Technically, Park's transformation is to the rotor reference frame, but the PMSM, is self-synchronous so we will use the term synchronous reference frame.

3.2 Stationary Reference Frame

Considering again the PMSM drive system for a moment, stationary reference frame control is shown in Figure 3-2.

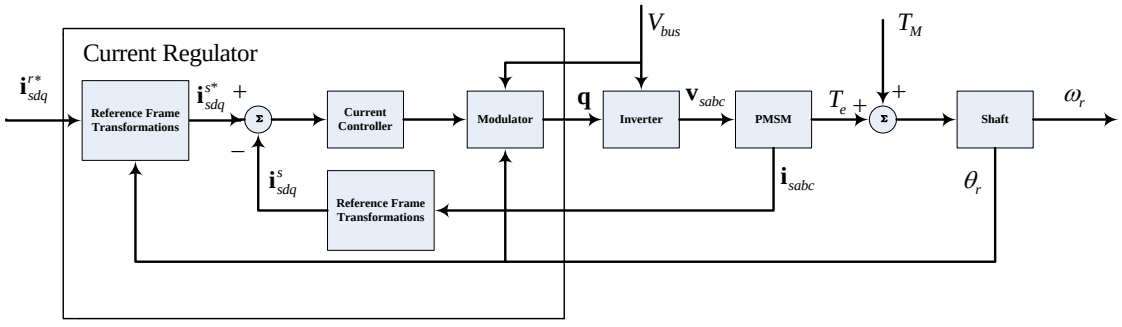

Figure 3-2. Block diagram of current control loop using stationary reference frame control.

3.2.1 Derivation of Closed-Loop Gain

Transforming (3.1) to the stationary reference frame and ignoring the zero-sequence variables, because the neutral of the stator winding is rarely connected, yields:

$$\begin{bmatrix} v_{sd}^s \\ v_{sq}^s \end{bmatrix} = \begin{bmatrix} R_s & 0 \\ 0 & R_s \end{bmatrix} \begin{bmatrix} i_{sd}^s \\ i_{sq}^s \end{bmatrix} + \begin{bmatrix} L_s & 0 \\ 0 & L_s \end{bmatrix} \frac{d}{dt} \begin{bmatrix} i_{sd}^s \\ i_{sq}^s \end{bmatrix} \tag{3.2}$$

where $L_s = L_{ls} + \frac{3}{2} L_{ms}$. This equation can be rewritten in a decoupled way as

$$v_{sd}^s = R_s i_{sd}^s + L_s \frac{d}{dt} i_{sd}^s \tag{3.3}$$

$$v_{sq}^s = R_s i_{sq}^s + L_s \frac{d}{dt} i_{sq}^s \tag{3.4}$$

Consequently, the stationary reference frame d- and q-axis currents can be controlled independently.

To obtain the closed-loop gain for i_{sd}^s and i_{sq}^s, we must first determine the transfer function of the RL circuit and the proportional controller separately.

The mathematical model for a single-phase RL circuit is:

$$R_s i + L_s \frac{d}{dt} i = v \tag{3.5}$$

For the d- and q-axis model in the s domain, this becomes:

$$(R_s + L_s s)\mathbf{I}_{sdq}^s(s) = \mathbf{V}_{sdq}^s(s) \tag{3.6}$$

The s domain representation of a Proportional controller is:

$$K_p \left(\mathbf{I}_{sdq}^{s*}(s) - \mathbf{I}_{sdq}^s(s) \right) = \mathbf{V}_{sdq}^s(s) \tag{3.7}$$

Replacing $\mathbf{V}_{sdq}^s(s)$ in (3.7) using the relationship between $\mathbf{I}_{sdq}^s(s)$ and $\mathbf{V}_{sdq}^s(s)$ in (3.6) yields:

$$\mathbf{I}_{sdq}^{s}(s) = \frac{K_p}{R_s + L_s s}(\mathbf{I}_{sdq}^{s*}(s) - \mathbf{I}_{sdq}^{s}(s)) \tag{3.8}$$

Solving for the closed-loop gain yields

$$G_{cl} = \frac{I_{sd}^{s}(s)}{I_{sd}^{s*}(s)} = \frac{I_{sq}^{s}(s)}{I_{sq}^{s*}(s)} = \frac{\dfrac{K_p}{K_p + R_s}}{\dfrac{L_s}{K_p + R_s} s + 1} \tag{3.9}$$

3.2.2 Analysis of Bandwidth Limitation

Equation (3.9) indicates that increasing K_p would increase the bandwidth of system and decrease the tracking error. Of course, one must always consider stability and limits on control effort. The root-locus for K_p is shown in Figure 3-3. All roots are located in the left half plane, which indicates this system is always stable.

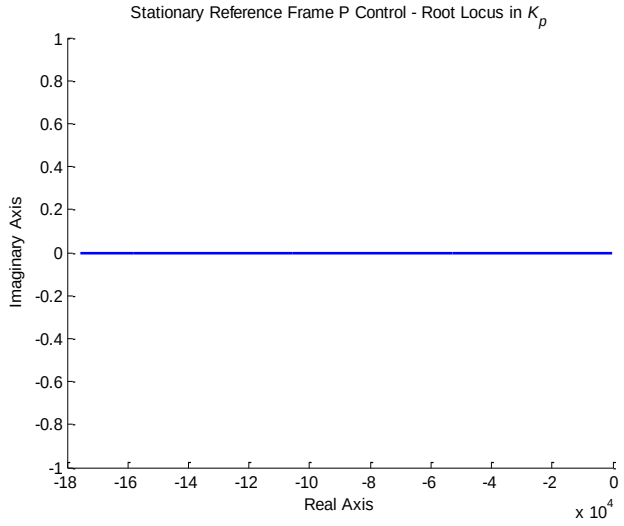

Figure 3-3. Root-locus plot for K_p of stationary reference frame proportional control.

However, because of the control effort limitation, K_p cannot be increased indefinitely to obtain wider bandwidth. To find a suitable K_p, bode plot like Figure 3-4 is drawn. Since when

the frequency is 800 Hz, magnitude of the bode plot reaches -3 dB, which would be called cutoff frequency, so to achieve a bandwidth of 800 Hz K_p is set to 30, which could also be verified by calculation:

$$\omega_c = \frac{R_s + K_p}{L_s} = \frac{(1.5+30)\times 10^3}{6.5} \text{ rad/s}$$
$$= \frac{31500}{6.5\times 6.2832} \text{ Hz} = 771 \text{ Hz}$$

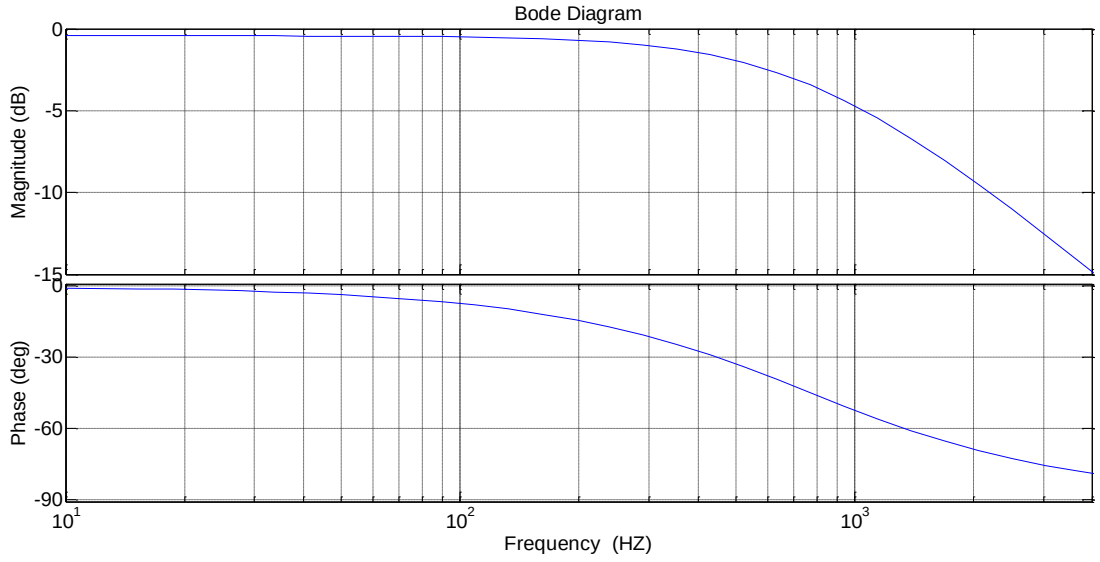

Figure 3-4. Bode plot of an ideal three-phase current regulator with stationary reference frame proportional control.

To verify the 800-Hz bandwidth of the stationary reference frame proportional control, the system was simulated using an ideal model for the inverter. The simulation results are shown in Figure 3-5 to 3-7. In Figures 3-5 and 3-6, the electrical frequency is set to 50 Hz and 500 Hz, respectively. Both are in the range of the 800 Hz bandwidth and the currents are controlled effectively. When the electrical frequency is increased to 1000 Hz, however, there is significant phase delay in the stationary reference frame variables that manifests itself as level errors in the synchronous reference frame.

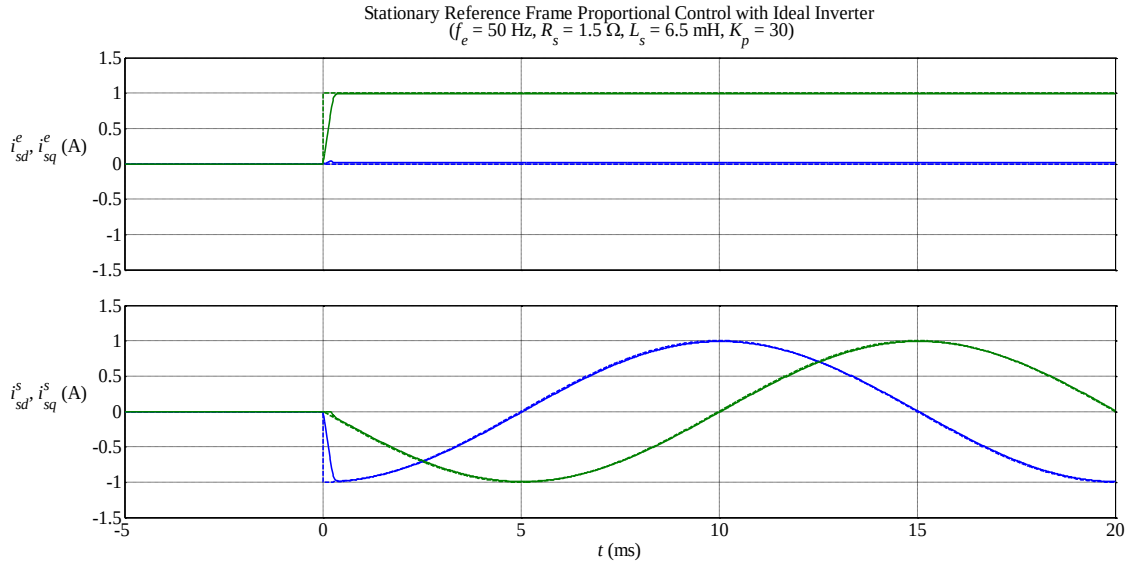

Figure 3-5. Simulation results for an ideal three-phase current controller using stationary reference frame proportional control with f_e = 50 Hz.

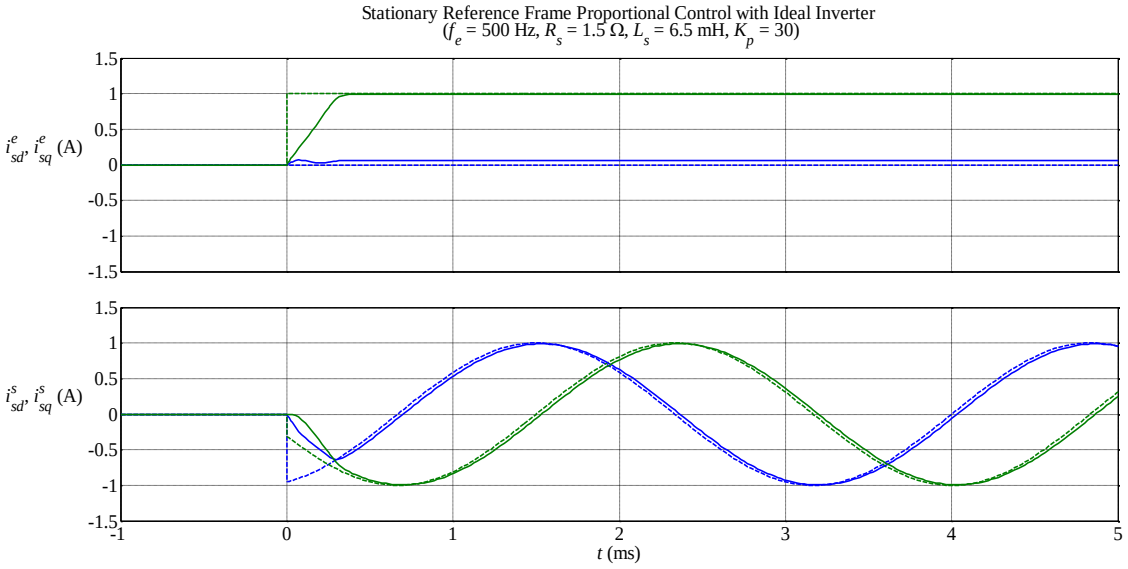

Figure 3-6. Simulation results for an ideal three-phase current controller using stationary reference frame proportional control with f_e = 500 Hz.

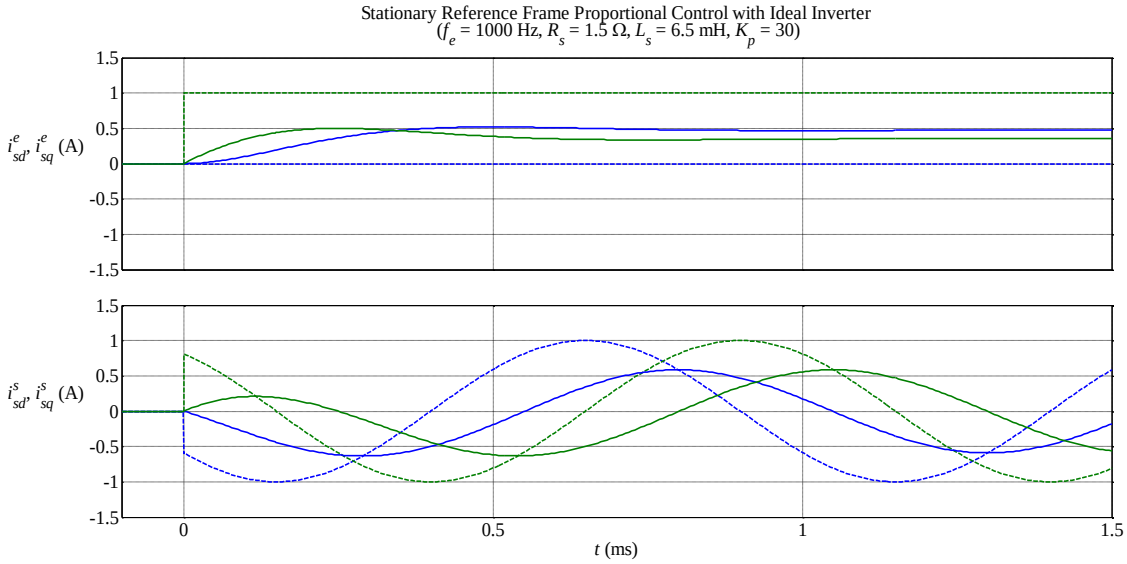

Figure 3-7. Simulation results for an ideal three-phase current controller using stationary reference frame proportional control with f_e = 1000 Hz.

In addition to the bandwidth limitation imposed by the choice of K_p, the inverter hardware has a significant effect on bandwidth. As a rule of thumb, the bandwidth of an inverter is usually assumed to be $\frac{1}{10}$ of the switching frequency. The effect of invert switching frequency is considered in Section 3.5.

3.3 Synchronous Reference Frame without EMF Compensation

Synchronous reference frame PI control was originally selected to avoid the bandwidth limitation imposed by the inverter hardware. More particularly, synchronous reference frame variables are dc (in the steady state) instead of ac. In this part, we derive the closed-loop transfer function for synchronous reference frame PI controller without emf compensation. From this we show that there is bandwidth limitation inherent to this control scheme.

A block diagram of current regulator loop using synchronous reference frame control is shown in Figure 3-8.

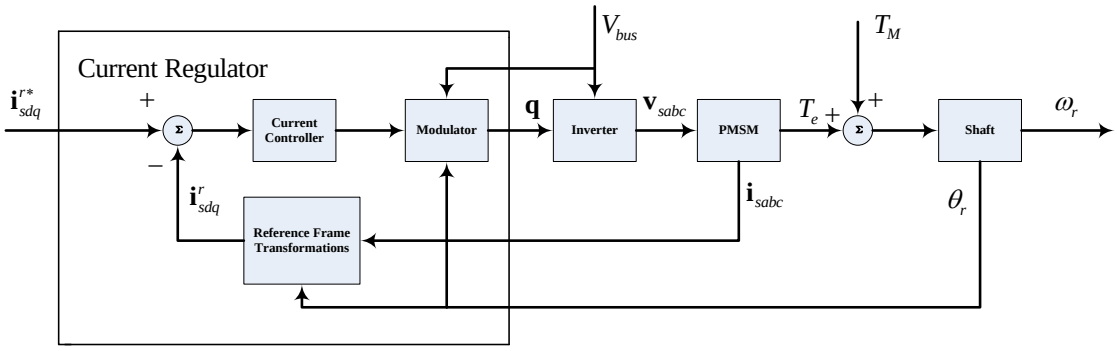

Figure 3-8. Block diagram of current control loop using synchronous reference frame control.

3.3.1 Derivation of Closed-Loop Gain

To analyze three-phase RL circuit currents, we first transform the plant model from the stationary reference frame in (3.3) to the synchronous reference frame which introduces a speed voltage term:

$$\begin{bmatrix} v^e_{sd} \\ v^e_{sq} \end{bmatrix} = \begin{bmatrix} R_s & 0 \\ 0 & R_s \end{bmatrix} \begin{bmatrix} i^e_{sd} \\ i^e_{sq} \end{bmatrix} + \begin{bmatrix} 0 & -\omega_e L_s \\ \omega_e L_s & 0 \end{bmatrix} \begin{bmatrix} i^e_{sd} \\ i^e_{sq} \end{bmatrix} + \begin{bmatrix} L_s & 0 \\ 0 & L_s \end{bmatrix} \frac{d}{dt} \begin{bmatrix} i^e_{sd} \\ i^e_{sq} \end{bmatrix} \tag{3.10}$$

or

$$\mathbf{v}^e_{sdq} = R_s \mathbf{I} \mathbf{i}^e_{sdq} + \omega_e L_s \mathbf{J} \mathbf{i}^e_{sdq} + L_s \mathbf{I} \frac{d}{dt} \mathbf{i}^e_{sdq} \tag{3.11}$$

where

$$\mathbf{I} = \begin{bmatrix} 1 & 0 \\ 0 & 1 \end{bmatrix}$$

$$\mathbf{J} = \begin{bmatrix} 0 & -1 \\ 1 & 0 \end{bmatrix}$$

In the s domain, the voltage equation (3.11) becomes:

$$\begin{aligned} \mathbf{V}^e_{sdq}(s) &= \left(R_s \mathbf{I} + \omega_e L_s \mathbf{J} + L_s \mathbf{I} s \right) \mathbf{I}^e_{sdq}(s) \\ &= \left[\left(R_s + L_s s \right) \mathbf{I} + \omega_e L_s \mathbf{J} \right] \mathbf{I}^e_{sdq}(s) \end{aligned} \tag{3.12}$$

To represent the PI controller here, (3.7) is first modified to be

$$\mathbf{V}_{sdq}^{e}(s)=\left(K_p+K_i\frac{1}{s}\right)\left(\mathbf{I}_{sdq}^{e*}(s)-\mathbf{I}_{sdq}^{e}(s)\right) \tag{3.13}$$

Equating $\mathbf{V}_{sdq}^{e}(s)$ in (3.12) and (3.13), it yields:

$$\left[(R_s+L_s s)\mathbf{I}+\omega_e L_s\mathbf{J}\right]\mathbf{I}_{sdq}^{e}(s)=\left(K_p+K_i\frac{1}{s}\right)\left(\mathbf{I}_{sdq}^{e*}(s)-\mathbf{I}_{sdq}^{e}(s)\right) \tag{3.14}$$

The closed-loop gain can then be derived as

$$\begin{aligned}\mathbf{G}_{cl}(\mathrm{s})&=\frac{\mathbf{I}_{sdq}^{e}(s)}{\mathbf{I}_{sdq}^{e*}(s)}\\&=\left[\left(L_s s^2+\left(K_p+R_s\right)s+K_i\right)\mathbf{I}+\omega_e L_s\mathbf{J}s\right]^{-1}\left(K_p s+K_i\right)\\&=\frac{\left(L_s K_p s^3+\left(K_p^2+R_s K_p+K_i L_s\right)s^2+K_i\left(2K_p+R_s\right)s+K_i^2\right)\mathbf{I}-\omega_e L_s\left(K_p s^2+K_i s\right)\mathbf{J}}{L_s^2 s^4+2L_s\left(K_p+R_s\right)s^3+\left(\left(K_p+R_s\right)^2+2K_i L_s+\left(\omega_e L_s\right)^2\right)s^2+2K_i\left(K_p+R_s\right)s+K_i^2}\end{aligned} \tag{3.15}$$

The matrices in the transfer function simply reflect the fact that there are four transfer functions from two inputs to two outputs:

$$\mathbf{G}_{cl}(s)=\begin{bmatrix}\dfrac{I_{sd}^{e}(s)}{I_{sd}^{e*}(s)} & \dfrac{I_{sd}^{e}(s)}{I_{sq}^{e*}(s)}\\[2ex]\dfrac{I_{sq}^{e}(s)}{I_{sd}^{e*}(s)} & \dfrac{I_{sq}^{e}(s)}{I_{sq}^{e*}(s)}\end{bmatrix}$$

$$\begin{aligned}\frac{I_{sd}^{e}(s)}{I_{sd}^{e*}(s)}&=\frac{I_{sq}^{e}(s)}{I_{sq}^{e*}(s)}\\&=\frac{L_s K_p s^3+(K_p^2+R_s K_p+K_i L_s)s^2+K_i(2K_p+R_s)s+K_i^2}{L_s^2 s^4+2L_s\left(K_p+R_s\right)s^3+\left(\left(K_p+R_s\right)^2+2K_i L_s+\left(\omega_e L_s\right)^2\right)s^2+2K_i\left(K_p+R_s\right)s+K_i^2}\end{aligned} \tag{3.16}$$

$$-\frac{I_{sq}^{e}(s)}{I_{sd}^{e*}(s)}=\frac{I_{sd}^{e}(s)}{I_{sq}^{e*}(s)}$$

$$=\frac{\omega_e L_s\left(K_p s^2+K_i s\right)}{L_s^2 s^4+2L_s\left(K_p+R_s\right)s^3+\left(\left(K_p+R_s\right)^2+2K_i L_s+\left(\omega_e L_s\right)^2\right)s^2+2K_i\left(K_p+R_s\right)s+K_i^2} \quad (3.17)$$

3.3.2 Analysis of Bandwidth Limitation

The poles of both transfer functions shown in (3.16) and (3.17) correspond to the roots of the shared denominator. For fixed K_p and ω_e, a root locus can be constructed by varying K_i from zero towards infinity. For $K_i = 0$, the denominator simplifies to:

$$den = L_s^2 s^4+2L_s\left(K_p+R_s\right)s^3+\left(\left(K_p+R_s\right)^2+\left(\omega_e L_s\right)^2\right)s^2$$

$$=s^2\left(s+\left(\frac{K_p+R_s}{L_s}-j\omega_e\right)\right)\left(s+\left(\frac{K_p+R_s}{L_s}+j\omega_e\right)\right)$$

Thus, the response includes a component that oscillates at frequency ω_e and decays with a time constant $L_s/(K_p+R_s)$. The root-locus for K_i is shown in Figure 3-9. Regarless of the value for K_i this system remains stable as all roots remain in the left plane. However, unlike the root locus for stationary reference frame control shown in Figure 3.3, the dominant poles approach an asymptote that limits bandwidth. The limit on bandwidth can be calculated as:

$$\omega_c=\frac{R_s+K_p}{2L_s}=\frac{(1.5+30)\times 10^3}{2\times 6.5}\ \text{rad/s}$$

$$=\frac{31500}{13\times 6.2832}\ \text{Hz}=386\ \text{Hz}$$

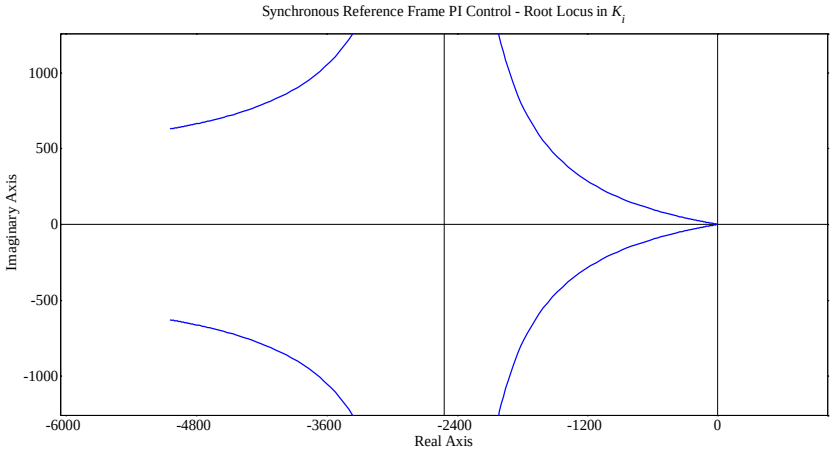

Figure 3-9. Root-locus plot for K_i of synchronous reference frame PI control.

3.4 Synchronous Reference Frame PI Control with EMF Compensation

From (3.11), it is important to note that the d- and q-axis voltage equations are coupled due to matrix **J**. To decouple the dynamics of the d- and q-axis currents and to counteract the oscillatory component, one useful method is to use EMF or speed-voltage compensation. That is, an EMF or speed-voltage term is added to the output of the PI control block.

There are two different ways to represent this EMF compensation—the actual d- and q-axis currents or the reference d- and q-axis currents —these two different equations are:

$$\mathbf{V}_{sdq}^{e}(s)=\left(K_p+K_i\frac{1}{s}\right)\left(\mathbf{I}_{sdq}^{e*}(s)-\mathbf{I}_{sdq}^{e}(s)\right)+\hat{\omega}_e\hat{L}_s\mathbf{J}\mathbf{I}_{sdq}^{e}(s) \quad \text{(actual currents)} \tag{3.18}$$

$$\mathbf{V}_{sdq}^{e}(s)=\left(K_p+K_i\frac{1}{s}\right)\left(\mathbf{I}_{sdq}^{e*}(s)-\mathbf{I}_{sdq}^{e}(s)\right)+\hat{\omega}_e\hat{L}_s\mathbf{J}\mathbf{I}_{sdq}^{e*}(s) \quad \text{(reference currents)} \tag{3.19}$$

where $\hat{\omega}_e$ is the estimation of ω_e and $\hat{L}_s$ is the estimate value of L_s.

3.4.1 Synchronous Reference Frame PI Control with Actual Current EMF

Using the same method applied before to derive an expression for the closed-loop gain, we equate two expressions for $\mathbf{V}_{sdq}^{e}(s)$: the plant model (3.13) and the controller model (3.18)

$$\left[(R_s + L_s s)\mathbf{I} + \omega_e L_s \mathbf{J}\right]\mathbf{I}_{sdq}^{e}(s) = \left(K_p + K_i \frac{1}{s}\right)\left(\mathbf{I}_{sdq}^{e*}(s) - \mathbf{I}_{sdq}^{e}(s)\right) + \hat{\omega}_e \hat{L}_s \mathbf{J}\mathbf{I}_{sdq}^{e}(s) \qquad (3.20)$$

Comparing this to (3.14), the only difference is that $\omega_e L_s$ in the former results for the synchronous reference frame PI control are replaced by $\omega_e L_s - \hat{\omega}_e \hat{L}_s$. Consequently, the closed-loop gain using the synchronous reference frame PI control with actual current EMF compensation would be obtained simply by replacing $\omega_e L_s$ in (3.16) and (3.17) by $\omega_e L_s - \hat{\omega}_e \hat{L}_s$:

$$\frac{I_{sq}^{e}(s)}{I_{sq}^{e*}(s)} = \frac{L_s K_p s^3 + (K_p^2 + R_s K_p + K_i L_s)s^2 + K_i(2K_p + R_s)s + K_i^2}{L_s^2 s^4 + 2L_s(K_p + R_s)s^3 + ((K_p + R_s)^2 + 2K_i L_s + (\omega_e L_s - \hat{\omega}_e \hat{L}_s)^2)s^2 + 2K_i(K_p + R_s)s + K_i^2} \qquad (3.21)$$

$$\frac{I_{sd}^{e}(s)}{I_{sq}^{e*}(s)} = \frac{(\omega_e L_s - \hat{\omega}_e \hat{L}_s)(K_p s^2 + K_i s)}{L_s^2 s^4 + 2L_s(K_p + R_s)s^3 + ((K_p + R_s)^2 + 2K_i L_s + (\omega_e L_s - \hat{\omega}_e \hat{L}_s)^2)s^2 + 2K_i(K_p + R_s)s + K_i^2} \qquad (3.22)$$

These closed-loop transfer functions can be verified by comparing the step response from the transfer function to that from the Simulink models. The results are shown in Figure 3-10 and confirm the correctness of the derivation.

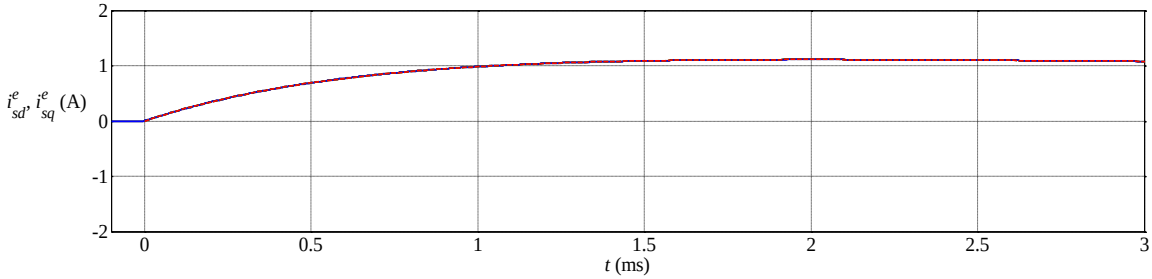

Figure 3-10. Comparison of step response of transfer function and simulation.

For the case of perfectly estimated values for ω_e and L_s, which means $\omega_e L_s - \hat{\omega}_e \hat{L}_s = 0$, the coupling between the d- and q-axis currents is eliminated, and the transfer function shared by the d- and q-axis currents simplifies to:

$$\frac{I_{sd}^{e}(s)}{I_{sd}^{e*}(s)} = \frac{I_{sq}^{e}(s)}{I_{sq}^{e*}(s)} = \frac{K_p s + K_i}{L_s s^2 + (K_p + R_s)s + K_i} \quad \text{(perfect estimation)} \tag{3.23}$$

For the case of imperfectly estimated values for ω_e and/or L_s, there will be complex conjugate roots even at $K_i = 0$, but the angular frequency of these roots will be:

$$\omega = \omega_e - \frac{\hat{\omega}_e \hat{L}_s}{L_s} \qquad (K_i = 0)$$

The root-locus for K_i is shown in Figure 3-11 and looks similar to Figure 3-9. Since $\hat{L}_s$ is in the denominator, with $\hat{L}_s$ changes from $0.9L_s$ to $1.1L_s$, the root-locus would be changed as shown in Figure 3-12. From root-locus in Figure 3-11 and 3-12, all poles are located in the left plane, indicating that the system is stable. And similar to Figure 3-9, as K_i increases, dominant poles move toward an asymptote that limits bandwidth. This limitation could be calculated as:

$$\omega_c = \frac{R_s + K_p}{2L_s} = \frac{(1.5+30)\times 10^3}{2\times 6.5} \text{ rad/s}$$
$$= \frac{31500}{13\times 6.2832} \text{ Hz} = 386 \text{ Hz}$$

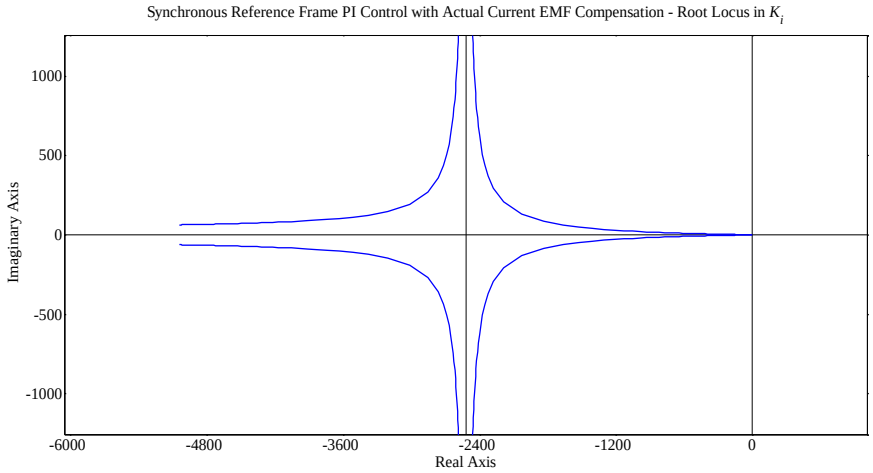

Figure 3-11. Root-locus for K_i in synchronous reference frame with actual current emf compensation.

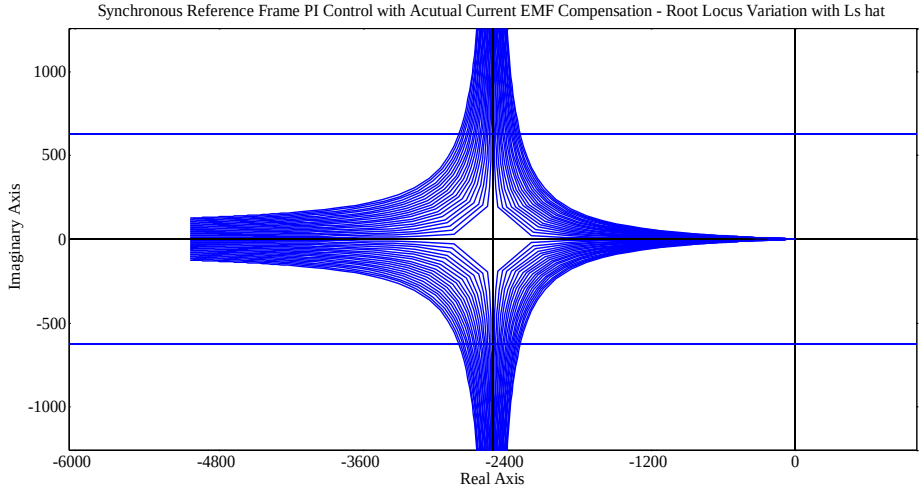

Figure 3-12. Root-locus with changed $\hat{L}_s$.

3.4.2 Synchronous Reference Frame PI Control with Reference Current EMF

As before, to acquire the closed-loop gain, we must equate two expressions for $\mathbf{V}^e_{sdq}(s)$, the voltage equation (3.19) and the PI controller model equation (3.13), which is shown below:

$$\left[(R_s + L_s s)\mathbf{I} + \omega_e L_s \mathbf{J}\right]\mathbf{I}^e_{sdq}(s) = \left(K_p + K_i \frac{1}{s}\right)\left(\mathbf{I}^{e*}_{sdq}(s) - \mathbf{I}^e_{sdq}(s)\right) + \hat{\omega}_e \hat{L}_s \mathbf{J}\mathbf{I}^{e*}_{sdq}(s) \qquad (3.24)$$

Add up all parameters before $\mathbf{I}_{sdq}^{e}(s)$ and $\mathbf{I}_{sdq}^{e*}(s)$ separately:

$$\left[\left(R_s + L_s s + K_p + K_i \frac{1}{s}\right)\mathbf{I} + \omega_e L_s \mathbf{J}\right]\mathbf{I}_{sdq}^{e}(s) = \left[\left(K_p + K_i \frac{1}{s}\right)\mathbf{I} + \hat{\omega}_e \hat{L}_s \mathbf{J}\right]\mathbf{I}_{sdq}^{e*}(s) \quad (3.25)$$

Representing $\mathbf{I}_{sdq}^{e}(s)$ using $\mathbf{I}_{sdq}^{e*}(s)$ yields:

$$\mathbf{I}_{sdq}^{e}(s) = \left[(L_s s^2 + (K_p + R_s)s + K_i)\mathbf{I} + \omega_e L_s \mathbf{J} s\right]^{-1}\left[(K_p s + K_i)\mathbf{I} + \hat{\omega}_e \hat{L}_s \mathbf{J} s\right]\mathbf{I}_{sdq}^{e*}(s) \quad (3.26)$$

The closed-loop gain is:

$$\begin{aligned}\mathbf{G}_{cl}(s) &= \frac{\mathbf{I}_{sdq}^{e}(s)}{\mathbf{I}_{sdq}^{e*}(s)} \\ &= \left[(L_s s^2 + (K_p + R_s)s + K_i)\mathbf{I} + \omega_e L_s \mathbf{J} s\right]^{-1}\left[(K_p s + K_i)\mathbf{I} + \hat{\omega}_e \hat{L}_s \mathbf{J} s\right]\end{aligned} \quad (3.27)$$

Carrying out the inversion of the first factor yields:

$$\mathbf{G}_{cl}(s) = \frac{(L_s s^2 + (K_p + R_s)s + K_i)\mathbf{I} - (\omega_e L_s s)\mathbf{J}}{(L_s s^2 + (K_p + R_s))^2 + (\omega_e L_s s)^2}((K_p s + K_i)\mathbf{I} + \hat{\omega}_e \hat{L}_s \mathbf{J} s) \quad (3.28)$$

Expanding the numerator and denominator into polynomials in *s* yields:

$$\mathbf{G}_{cl}(s) = \frac{(L_s K_p s^3 + (K_p^2 + R_s K_p + K_i L_s + \omega_e L_s \hat{\omega}_e \hat{L}_s)s^2 + K_i(2K_p + R_s)s + K_i^2)\mathbf{I} + (\hat{\omega}_e \hat{L}_s L_s s^3 + (\hat{\omega}_e \hat{L}_s R_s + K_p(\hat{\omega}_e \hat{L}_s - \omega_e L_s))s^2 + K_i(\hat{\omega}_e \hat{L}_s - \omega_e L_s)s)\mathbf{J}}{L_s^2 s^4 + 2L_s(K_p + R_s)\ s^3 + ((K_p + R_s)^2 + 2K_i L_s + (\omega_e L_s)^2)s^2 + 2K_i(K_p + R_s)s + K_i^2}$$

As mentioned before, although the matrices in the transfer function reflect the fact that there are four transfer functions from two inputs to two outputs as above, what we are really concerned about is:

$$\begin{aligned}\frac{I_{sd}^{e}(s)}{I_{sd}^{e*}(s)} &= \frac{I_{sq}^{e}(s)}{I_{sq}^{e*}(s)} \\ &= \frac{L_s K_p s^3 + (K_p^2 + R_s K_p + K_i L_s + \omega_e L_s \hat{\omega}_e \hat{L}_s)s^2 + K_i(2K_p + R_s)s + K_i^2}{L_s^2 s^4 + 2L_s K_p + R_s s^3 + ((K_p + R_s)^2 + 2K_i L_s + (\omega_e L_s)^2)s^2 + 2K_i(K_p + R_s)s + K_i^2}\end{aligned} \quad (3.29)$$

$$\frac{I_{sq}^{e}(s)}{I_{sd}^{e*}(s)} = -\frac{I_{sd}^{e}(s)}{I_{sq}^{e*}(s)}$$

$$= \frac{\hat{\omega}_e \hat{L}_s L_s s^3 + (\hat{\omega}_e \hat{L}_s R_s + K_p(\hat{\omega}_e \hat{L}_s - \omega_e L_s))s^2 + K_i(\hat{\omega}_e \hat{L}_s - \omega_e L_s)s}{L_s^2 s^4 + 2L_s K_p + R_s s^3 + ((K_p + R_s)^2 + 2K_i L_s + (\omega_e L_s)^2)s^2 + 2K_i(K_p + R_s)s + K_i^2} \tag{3.30}$$

Again comparing the step response from (3.30) and from the Simulink model as shown in Figure 3-13 confirms the correctness of the derivation.

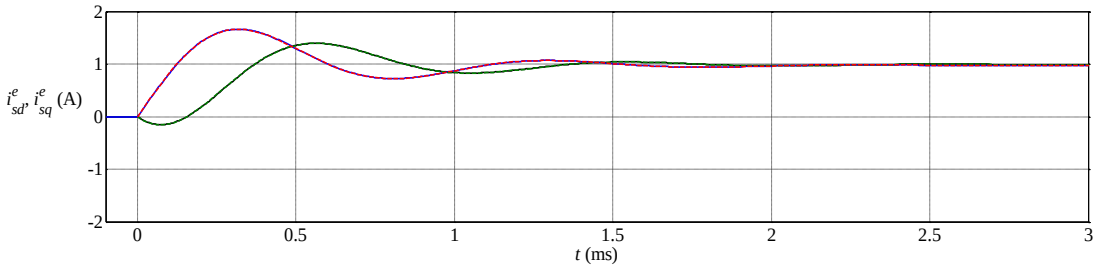

Figure 3-13. Comparison of step response of transfer function and simulation.

Comparing (3.29) & (3.30) to (3.16) & (3.17), these closed-loop transfer functions share the same denominator, so that the root locus should be the same when varying K_i from zero towards infinity.

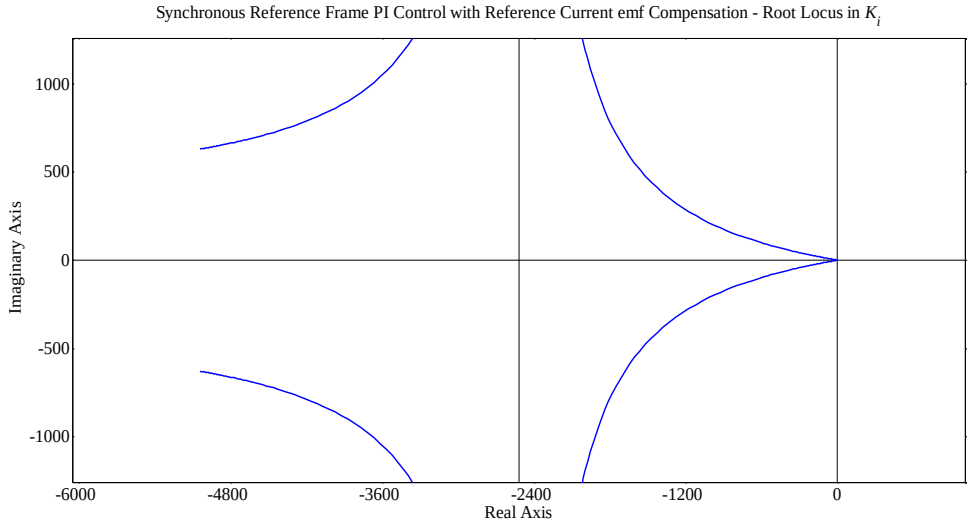

Figure 3-14. Root-locus plot for K_i in synchronous reference frame with reference current emf compensation.

From Figure 3-14, the system is stable, as all poles remain in the left half plane. As K_i is increased, the dominant poles move towards a fixed asymptote, which implies a bandwidth limitation. Since there is no $\hat{L}_s$ in the denominator of this closed-loop transfer function, unlike the former one, the root-locus for different values of $\hat{L}_s$ is no longer needed.

3.5 Non-Ideal Inverter Simulation

For all of the synchronous reference frame PI control methods we have discussed before, including one without EMF compensation, with reference current EMF compensation and with actual current EMF compensation, only the last one could control d- and q- currents separately. So in this part, only synchronous reference frame PI control with actual current EMF compensation is analyzed and compared to stationary reference frame proportional control.

Since the carrier frequency is 2 kHz, according to the one-tenth rule of thumb, the bandwidth of this system would be approximately 200 Hz. From Figure 3-16 and 3-18, by using stationary reference frame proportional control, currents would not reach their goal when $f_e = 200\ \text{Hz}$, while using synchronous reference frame PI control, this restriction would be eliminated. What's more, from Figure 3-15 and 3-17, when f_e is lower, synchronous reference frame PI control could produce a better output. And these are the reasons why low frequency synchronous reference frame PI control is widely used.

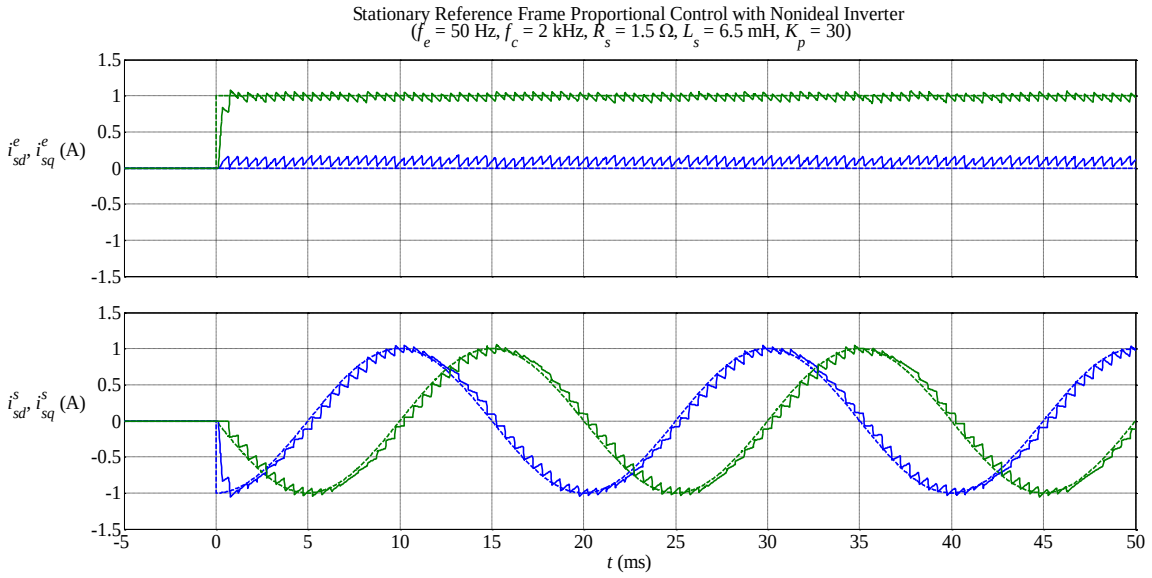

Figure 3-15. Simulation results for three-phase current controller using stationary reference frame proportional control with f_e = 50 Hz and 2-kHz switching.

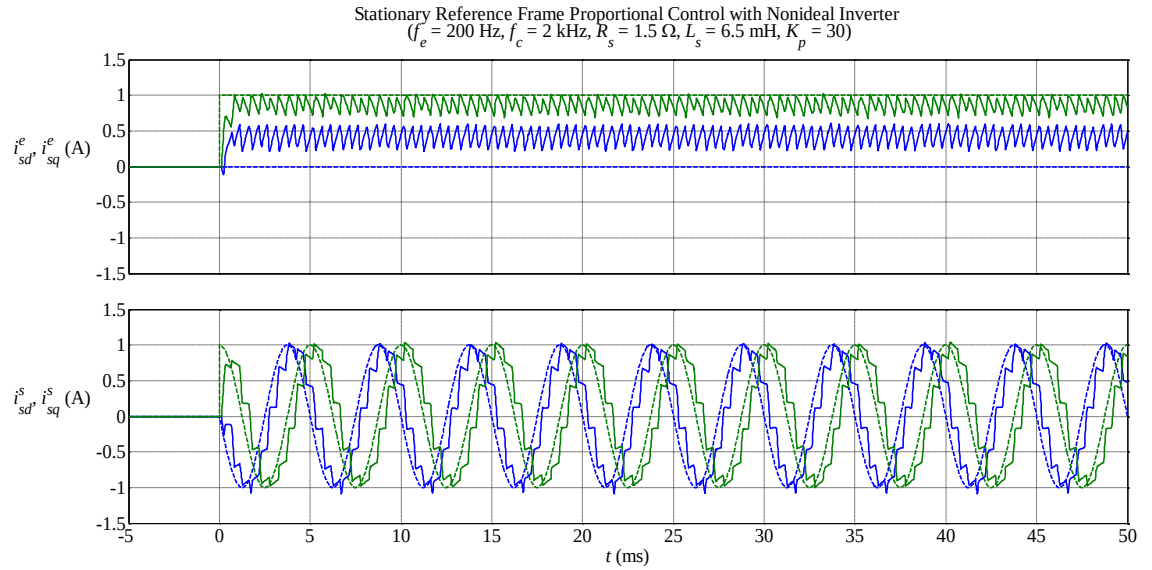

Figure 3-16. Simulation results for three-phase current controller using stationary reference frame proportional control with f_e = 200 Hz and 2-kHz switching.

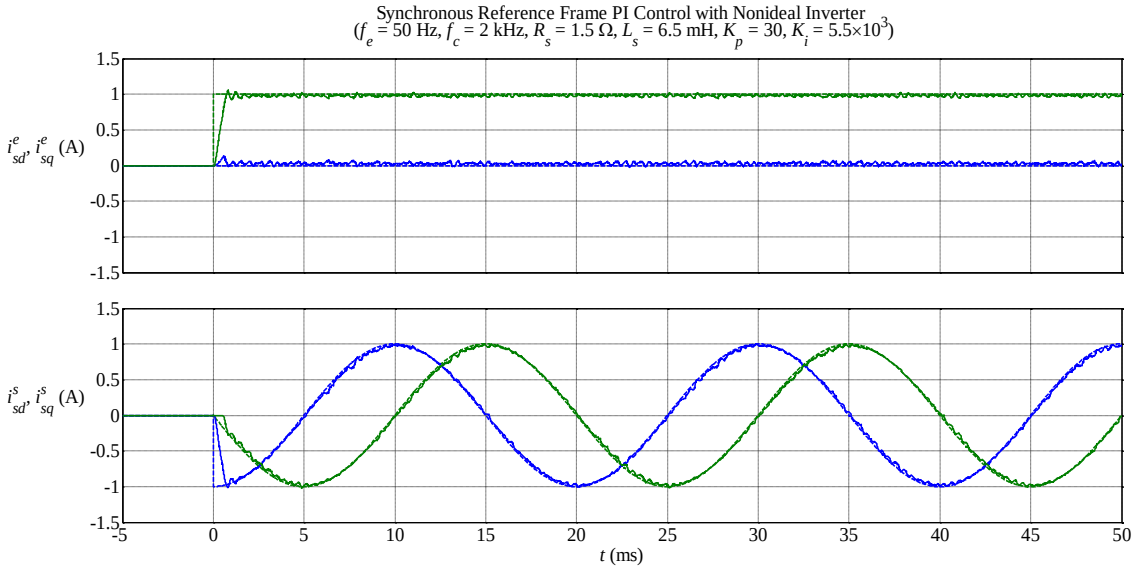

Figure 3-17. Simulation results for three-phase current controller using synchronous reference frame PI control with f_e = 50 Hz and 2-kHz switching..

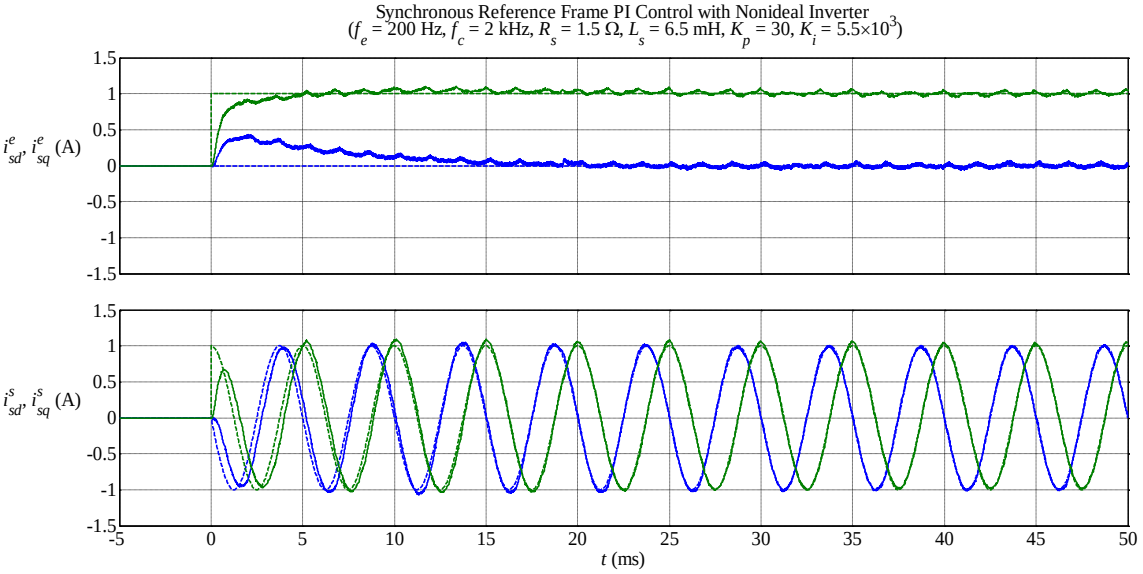

Figure 3-18. Simulation results for three-phase current controller using synchronous reference frame PI control with f_e = 200 Hz and 2-kHz switching.

To demonstrate that synchronous reference frame PI control avoids the bandwidth limitation imposed by hardware but has a bandwidth limitation of its own, several simulations

were performed with different synchronous frequencies and switching frequencies. The results with are shown in Figure 3-19 to 3-22.

By comparing Figure 3-19 and 3-21, still, synchronous reference frame PI control would bring better current response than the other one at low frequency (50 Hz). However, because of the bandwidth limitation set by its own mathematical equation, as soon as frequency is higher than this restriction (386 Hz in this case), synchronous reference frame PI control does not perform well. This is demonstrated by Figure 3-20 and 3-22, when f_e = 500 Hz.

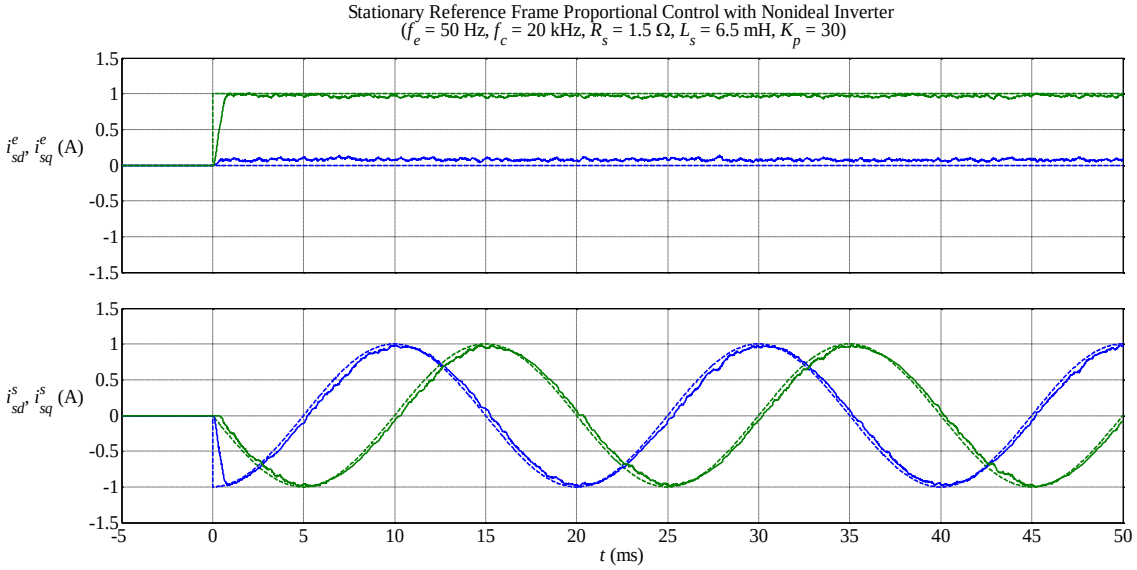

Figure 3-19. Simulation results for three-phase current controller using stationary reference frame proportional control with f_e = 50 Hz and 20-kHz switching.

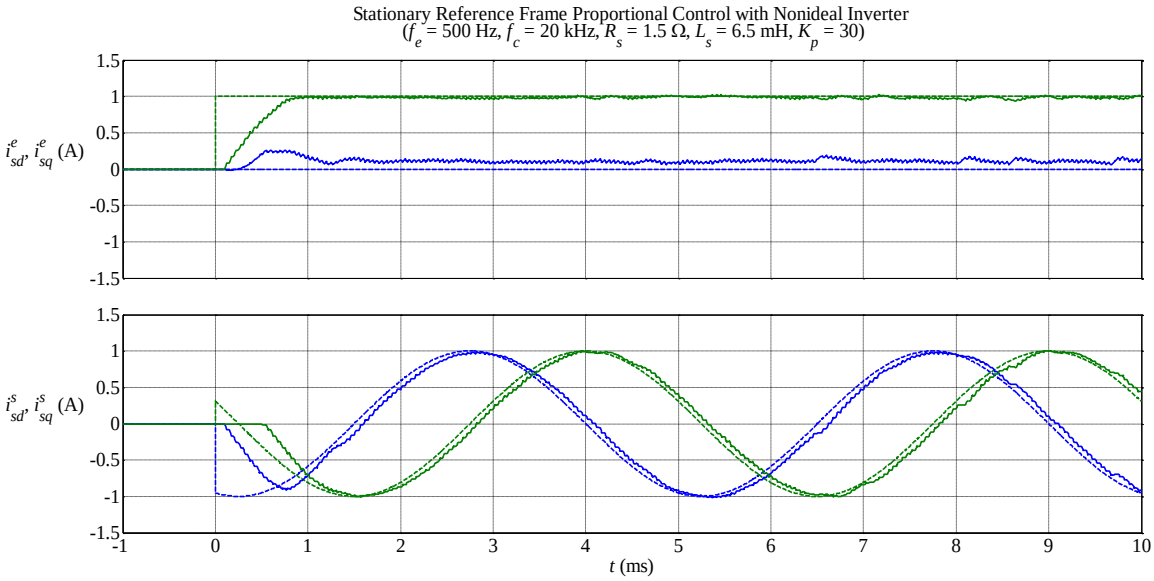

Figure 3-20. Simulation results for three-phase current controller using stationary reference frame proportional control with f_e = 500 Hz and 20-kHz switching..

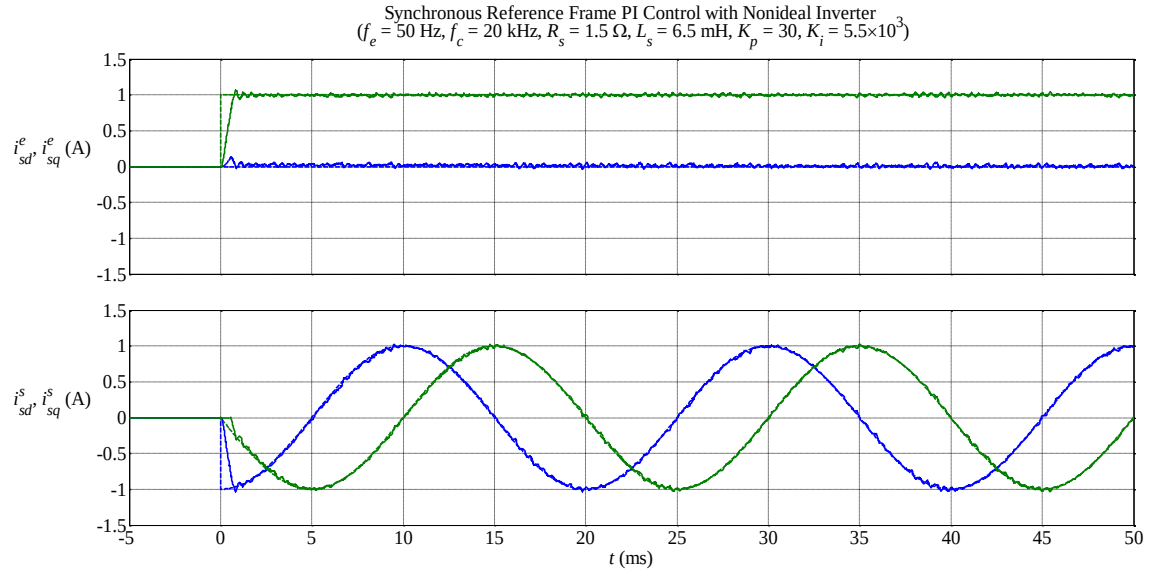

Figure 3-21. Simulation results for three-phase current controller using synchronous reference frame PI control with f_e = 50 Hz and 20-kHz switching.

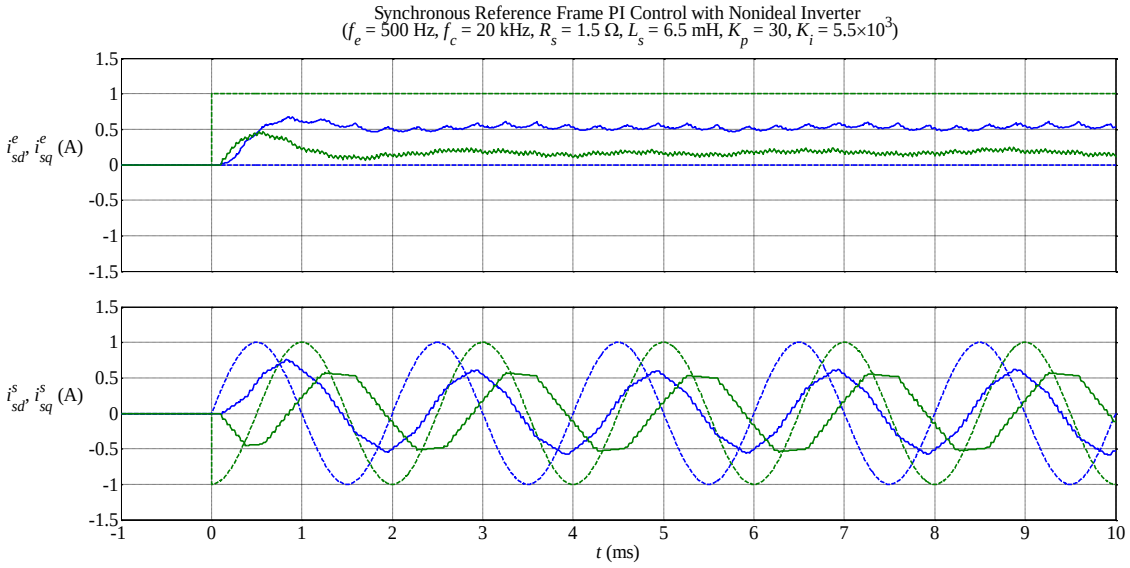

Figure 3-22. Simulation results for three-phase current controller using synchronous reference frame PI control with f_e = 500 Hz and 20-kHz switching.

3.6 Conclusion

Bandwidth limitations for stationary reference frame proportional control and synchronous reference frame PI control have been derived via analysis of transfer functions for the closed loop system taking reference frame transformations into account. As expected, synchronous reference frame PI control outperforms stationary reference frame proportional control when the hardware bandwidth is relatively low and the synchronous (electrical) frequency is low. When the hardware bandwidth is high, however, synchronous reference frame PI control is unable to take advantage of it, whereas stationary reference frame proportional control is. The impact of tracking error associated with stationary reference frame proportional control is examined in the next chapter.

Chapter 4

Effect of Current Control Method on Velocity Control of a Permanent Magnet Synchronous Machine Drive System

In Chapter 3, we analyzed the current control for a three-phase RL circuit. Among the different current regulation methods using synchronous reference frame PI control, including the one without EMF compensation, with actual or reference current EMF, synchronous reference frame PI control with actual current EMF compensation would not only produce a more stable output, but also decouple currents to make them easier to control. However, because of its own mathematical derivation, there would exist a bandwidth limitation while using stationary reference frame Proportional control could ignore this restriction. Still, using stationary reference frame Proportional control could also regulate current properly. In this chapter, we intend to find out the effect of these methods on the velocity response of a PMSM.

4.1 Stationary Reference Frame

With the reference frame transformation shown in (4.1) and (4.2), d- and q- variables in stationary reference frame and synchronous reference frame could be transformed:

$$f_{sd}^{s} = f_{sd}^{r}\cos(\theta_r) - f_{sq}^{r}\sin(\theta_r) \tag{4.1}$$

$$f_{sq}^{s} = f_{sd}^{r}\sin(\theta_r) + f_{sq}^{r}\cos(\theta_r) \tag{4.2}$$

where f could be *v*, *i* or λ .

Using these transformations, (4.3), current-voltage equation in synchronous reference frame by equating (2.7) and (2.8) can be written in forms of (4.4) and (4.5):

$$\mathbf{v}^{r}_{sdq0} = \mathbf{r}_s \mathbf{i}^{r}_{sdq0} + \omega_r \mathbf{J}(\mathbf{L}^{r}_{s}\mathbf{i}^{r}_{sdq0} + \boldsymbol{\lambda}'^{r}_{sm}) + \frac{d}{dt}(\mathbf{L}^{r}_{s}\mathbf{i}^{r}_{sdq0} + \boldsymbol{\lambda}'^{r}_{sm}) \tag{4.3}$$

$$\begin{aligned} v^{s}_{sd} &= r_s i^{s}_{sd} + L_s \frac{d}{dt} i^{s}_{sd} + \omega_r \lambda'_{sm}\left[-\tfrac{2}{3}\sin(\theta_r) + \tfrac{1}{3}\sin(\theta_r - \tfrac{2}{3}\pi) + \tfrac{1}{3}\sin(\theta_r + \tfrac{2}{3}\pi)\right] \\ &= r_s i^{s}_{sd} + L_s \frac{d}{dt} i^{s}_{sd} - \omega_r \lambda'_{sm}\sin(\theta_r) \end{aligned} \tag{4.4}$$

$$\begin{aligned} v^{s}_{sq} &= r_s i^{s}_{sq} + L_s \frac{d}{dt} i^{s}_{sq} + \omega_r \lambda'_{sm}\left[-\tfrac{\sqrt{3}}{3}\sin(\theta_r - \tfrac{2}{3}\pi) + \tfrac{\sqrt{3}}{3}\sin(\theta_r + \tfrac{2}{3}\pi)\right] \\ &= r_s i^{s}_{sq} + L_s \frac{d}{dt} i^{s}_{sq} + \omega_r \lambda'_{sm}\cos(\theta_r) \end{aligned} \tag{4.5}$$

The time domain representation of the proportional controller is:

$$K_p\left(i^{s^*}_{sd} - i^{s}_{sd}\right) = v^{s}_{sd} \tag{4.6}$$

$$K_p\left(i^{s^*}_{sq} - i^{s}_{sq}\right) = v^{s}_{sq} \tag{4.7}$$

Combining (4.4) with (4.6) and (4.5) with (4.7) individually yields:

$$K_p\left(i^{s^*}_{sd} - i^{s}_{sd}\right) = r_s i^{s}_{sd} + L_s \frac{d}{dt} i^{s}_{sd} - \omega_r \lambda'_{sm}\sin(\theta_r) \tag{4.8}$$

$$K_p\left(i^{s^*}_{sq} - i^{s}_{sq}\right) = r_s i^{s}_{sq} + L_s \frac{d}{dt} i^{s}_{sq} + \omega_r \lambda'_{sm}\cos(\theta_r) \tag{4.9}$$

Applying (4.1) and (4.2) while assuming $i^{r^*}_{sd}(s) = 0$:

$$i^{s^*}_{sd} = i^{r^*}_{sd}\cos(\theta_r) - i^{r^*}_{sq}\sin(\theta_r) = -i^{r^*}_{sq}\sin(\theta_r) \tag{4.10}$$

$$i^{s^*}_{sq} = i^{r^*}_{sd}\sin(\theta_r) + i^{r^*}_{sq}\cos(\theta_r) = i^{r^*}_{sq}\cos(\theta_r) \tag{4.11}$$

A similar process also applies to i^{s}_{sd} and i^{s}_{sq}. Substituting (4-10) and (4-11) into (4.8) and (4.9) yields:

$$-K_p i_{sq}^{r*}\sin(\theta_r)-\left(K_p+r_s\right)\left(-i_{sq}^{r}\sin(\theta_r)\right)=L_s\frac{d}{dt}\left(-i_{sq}^{r}\sin(\theta_r)\right)-\omega_r\lambda'_{sm}\sin(\theta_r) \quad (4.12)$$

$$K_p i_{sq}^{r*}\cos(\theta_r)-\left(K_p+r_s\right)\left(i_{sq}^{r}\cos(\theta_r)\right)=L_s\frac{d}{dt}\left(i_{sq}^{r}\cos(\theta_r)\right)+\omega_r\lambda'_{sm}\cos(\theta_r) \quad (4.13)$$

After applying the product rule of differentiation these two equations become:

$$-K_p i_{sq}^{r*}\sin(\theta_r)-\left(K_p+r_s\right)\left(-i_{sq}^{r}\sin(\theta_r)\right)=L_s\left(-\sin(\theta_r)\frac{d}{dt}i_{sq}^{r}-\omega_r\cos(\theta_r)i_{sq}^{r}\right)-\omega_r\lambda'_{sm}\sin(\theta_r) \quad (4.14)$$

$$K_p i_{sq}^{r*}\cos(\theta_r)-\left(K_p+r_s\right)\left(i_{sq}^{r}\cos(\theta_r)\right)=L_s\left(\cos(\theta_r)\frac{d}{dt}i_{sq}^{r}-\omega_r\sin(\theta_r)i_{sq}^{r}\right)+\omega_r\lambda'_{sm}\cos(\theta_r) \quad (4.15)$$

Subtracting (4.15) from (4.14), and then multiplying by $\tan\left(\theta_r\right)$ yields:

$$\begin{aligned}&K_p i_{sq}^{r*}\left(\cos^2(\theta_r)+\sin^2(\theta_r)\right)-\left(K_p+r_s\right)i_{sq}^{r}\left(\cos^2(\theta_r)+\sin^2(\theta_r)\right)\\&=L_s\frac{d}{dt}i_{sq}^{r}\left(\cos^2(\theta_r)+\sin^2(\theta_r)\right)+\omega_r\lambda'_{sm}\left(\cos^2(\theta_r)+\sin^2(\theta_r)\right)\end{aligned} \quad (4.16)$$

Since $\cos^2(\theta_r)+\sin^2(\theta_r)\equiv 1$, this factor can be eliminated. Then (4.16) can be represented in *s* domain:

$$\left(K_p+r_s+sL_s\right)I_{sq}^{r}(s)=-\omega_r\lambda'_{sm}+K_p I_{sq}^{r*}(s) \quad (4.17)$$

The s-domain form of (2.10) is

$$s\omega_r=\frac{P}{2}\frac{1}{J}\left(\frac{P}{2}\frac{3}{2}\lambda'_{sm}I_{sq}^{r}(s)-T_M-D\frac{P}{2}\omega_r\right) \quad (4.18)$$

Substituting $I_{sq}^{r}(s)$ in (4.18) with relationship shown in (4.17), it yields:

$$s\omega_r=\frac{P}{2}\frac{1}{J}\left[\frac{P}{2}\lambda'_{sm}\left(-\frac{3}{2}\right)\left(\frac{\omega_r\lambda'_{sm}-K_p I_{sq}^{r*}(s)}{r_s+K_p+sL_s}\right)-T_M-D\frac{P}{2}\omega_r\right] \quad (4.19)$$

By collecting terms multiplying ω_r and $I_{sq}^{r*}(s)$ respectively, (4.19) becomes:

$$\left[sr_s + sK_p + s^2 L_s + \frac{3P^2 \lambda'^2_{sm}}{8J} + \frac{AP}{2J}\left(r_s + K_p + sL_s\right) + \frac{DP^2}{4J}\left(r_s + K_p + sL_s\right) \right] \omega_r = \frac{3P^2 \lambda'_{sm} K_p}{8J} I^{r*}_{sq}(s) \tag{4.20}$$

Thus, the gain from $I^{r*}_{sq}(s)$ to ω_r can be expressed as:

$$\frac{\omega_r}{I^{r*}_{sq}} = \frac{3P^2 \lambda'_{sm} K_p}{8JL_s s^2 + \left[8J\left(K_p + r_s\right) + 2P^2 DL_s + 4PAL_s\right]s + \left[\left(2P^2 D + 4PA\right)\left(K_p + r_s\right) + 3P^2 \lambda'^2_{sm}\right]} \tag{4.21}$$

When using a PI controller for velocity, the reference q-axis current in the rotor reference frame is

$$I^{r*}_{sq} = \left(\bar{K}_p + \frac{\bar{K}_i}{s}\right)\left(\omega^*_r - \omega_r\right) \tag{4.22}$$

where $\bar{K}_p$ (and $\bar{K}_i$) is used here to distinguish it from the proportional gain K_p of the current controller.

Substituting I^{r*}_{sq} in (4.21) using (4.22) yields:

$$\frac{\omega_r}{\left(\bar{K}_p + \frac{\bar{K}_i}{s}\right)\left(\omega^*_r - \omega_r\right)} = \frac{3P^2 \lambda'_{sm} K_p}{8JL_s s^2 + \left[8J\left(K_p + r_s\right) + 2P^2 DL_s + 4PAL_s\right]s + \left[\left(2P^2 D + 4PA\right)\left(K_p + r_s\right) + 3P^2 \lambda'^2_{sm}\right]} \tag{4.23}$$

Using cross-multiplication and multiplied by s with all coefficients, (4.23) would become:

$$\left\{8JL_s s^3 + \left[8J\left(K_p + r_s\right) + 2P^2 DL_s + 4PAL_s\right]s^2 + \left[\left(2P^2 D + 4PA\right)\left(K_p + r_s\right) + 3P^2 \lambda'^2_{sm}\right]s\right\}\omega_r = 3P^2 \lambda'_{sm} K_p \left(\bar{K}_p s + \bar{K}_i\right)\left(\omega^*_r - \omega_r\right)$$

(4.24)

Adding up all coefficients before ω_r and ω_r^* respectively, the closed-loop gain could then be:

$$\frac{\omega_r}{\omega_r^*} = \frac{3P^2\lambda'_{sm}K_p\bar{K}_p s + P^2\lambda'_{sm}K_p\bar{K}_i}{d_3 s^3 + d_2 s^2 + d_1 s + d_0} \tag{4.25}$$

where

$$d_3 = 8JL_s$$

$$d_2 = 8J\left(K_p + r_s\right) + 2P^2DL_s + 4PAL_s$$

$$d_3 = \left(2P^2D + 4PA\right)\left(K_p + r_s\right) + 3P^2\lambda'^2_{sm} + 3P^2\lambda'_{sm}K_p\bar{K}_p$$

$$d_0 = 3P^2\lambda'_{sm}K_p\bar{K}_i$$

To verify the derivation of (4.25), its step response is compared to the ratio of the actual velocity over reference velocity from a time-domain simulation in Figure 4-1.

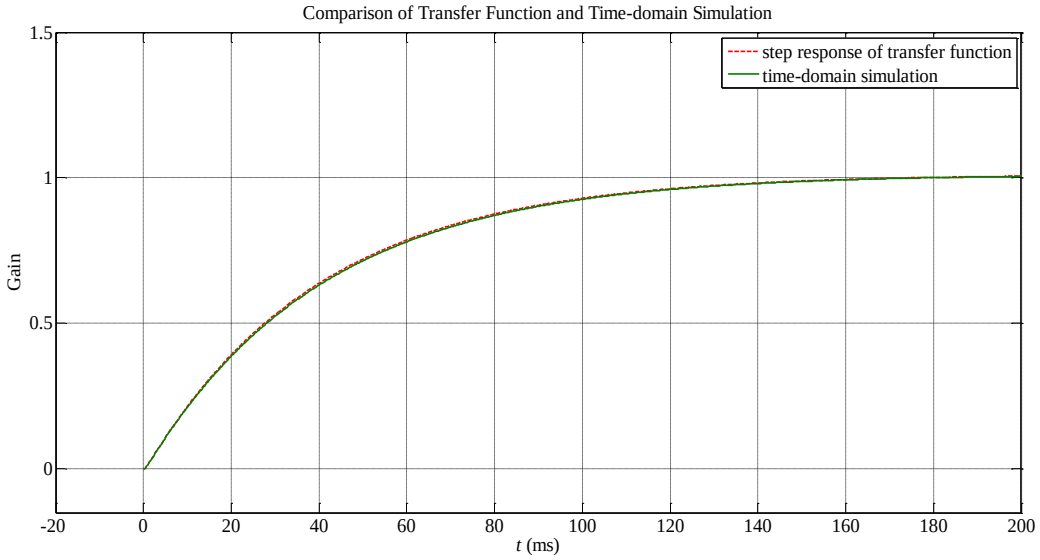

Figure 4-1. Comparison of transfer function and time-domain simulation.

After substituting PMSM parameters in Table 2-1, root-locus of (4.25) could be drawn as in Figure 4-2:

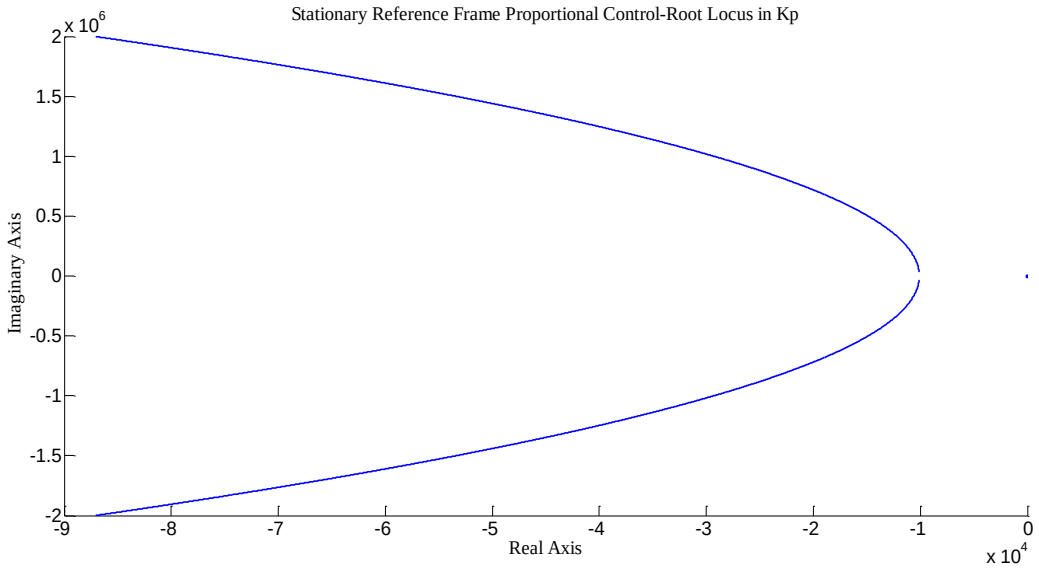

Figure 4-2. Root-locus for K_p of stationary reference frame proportional control.

Since all roots of the denominator are located in the left half plane, as shown in Figure 4-2, the system is stable. Also, as K_p increases from 0 to infinity, the dominant poles of (4.25) move away from imaginary axis, leading to an increase in bandwidth. The only problem would be that control effort of K_p might restrict this bandwidth as discussed in Chapter 3.

4.2 Synchronous Reference Frame

As shown before, (4.3) is derived as below:

$$\mathbf{v}_{sdq0}^{r} = \mathbf{r}_s \mathbf{i}_{sdq0}^{r} + \omega_r \mathbf{J}(\mathbf{L}_s^{r} \mathbf{i}_{sdq0}^{r} + \boldsymbol{\lambda}_{sm}^{\prime r}) + \frac{d}{dt}(\mathbf{L}_s^{r} \mathbf{i}_{sdq0}^{r} + \boldsymbol{\lambda}_{sm}^{\prime r}) \tag{4.26}$$

Since $\boldsymbol{\lambda}_{sm}^{\prime r}$ is a constant, $d\boldsymbol{\lambda}_{sm}^{\prime r} / dt = 0$. Written in non-vector form, this voltage-current equation is then comprised of the following two equations:

$$v_{sd}^{r} = r_s i_{sd}^{r} - \omega_r L_q i_{sq}^{r} + \frac{d}{dt} L_d i_{sd}^{r} \tag{4.27}$$

$$v_{sq}^{r} = r_s i_{sq}^{r} + \omega_r L_d i_{sd}^{r} + \omega_r \lambda_{sm}^{\prime r} + \frac{d}{dt} L_q i_{sq}^{r} \tag{4.28}$$

4.2.1 Transfer Function Derivation

To derive the transfer function of the close-loop system, we used the same method that was introduced in Chapter 3 and rewrite the voltage-current equation and PI controller equation in the *s* domain. By equating these equations we were able to obtain the relationship between actual current and reference current.

4.2.1.1 Synchronous Reference Frame PI Control without EMF Compensation

The mathematical expression for the PI controller in the *s* domain is similar to (3.6):

$$\left(K_p + \frac{K_i}{s}\right)\left(\mathbf{I}_{sdq}^{r*}(s) - \mathbf{I}_{sdq}^{r}(s)\right) = \mathbf{V}_{sdq}^{r}(s) \tag{4.29}$$

Equation (4.29) can be rewritten in scalar form as:

$$\left(K_p + \frac{K_i}{s}\right)\left(I_{sd}^{r*}(s) - I_{sd}^{r}(s)\right) = V_{sd}^{r}(s) \tag{4.30}$$

$$\left(K_p + \frac{K_i}{s}\right)\left(I_{sq}^{r*}(s) - I_{sq}^{r}(s)\right) = V_{sq}^{r}(s) \tag{4.31}$$

Equations (4.24) and (4.25) in the *s* domain are

$$V_{sd}^{r}(s) = r_s I_{sd}^{r}(s) - \omega_r L_q I_{sq}^{r}(s) + sL_d I_{sd}^{r}(s) \tag{4.32}$$

$$V_{sq}^{r}(s) = r_s I_{sq}^{r}(s) + \omega_r L_d I_{sd}^{r}(s) + sL_d I_{sq}^{r}(s) + \omega_r \lambda_{sm}^{\prime r} \tag{4.33}$$

Assuming $I_{sd}^{r*}(s) = 0$ and equating (4.30) and (4.32) yields

$$\left(r_s + sL_d + K_p + \frac{K_i}{s}\right) I_{sd}^r(s) = \omega_r L_q I_{sq}^r(s) \tag{4.34}$$

Similarly, equating (4.31) and (4.33) yields

$$\left(r_s + sL_q + K_p + \frac{K_i}{s}\right) I_{sq}^r(s) + \omega_r L_d I_{sd}^r(s) + \omega_r \lambda_{sm}'^r = \left(K_p + \frac{K_i}{s}\right) I_{sq}^{r*}(s) \tag{4.35}$$

Replacing $I_{sd}^r(s)$ in (4.34) by $I_{sq}^r(s)$ using the relationship between these two shown in (4.35):

$$\left[\left(r_s + sL_q + K_p + \frac{K_i}{s}\right) + \frac{\omega_r^2 L_d L_q}{r_s + sL_d + K_p + \frac{K_i}{s}}\right] I_{sq}^r(s) + \omega_r \lambda_{sm}'^r = \left(K_p + \frac{K_i}{s}\right) I_{sq}^{r*}(s) \tag{4.36}$$

Rewrite (4.18) as below:

$$\left[s + \left(\frac{P}{2}\right)^2 \frac{D}{J} + \frac{PA}{2J}\right] \omega_r = \left(\frac{P}{2}\right)^2 \frac{1}{J}\frac{3}{2} \lambda_{sm}' I_{sq}^r(s) \tag{4.37}$$

Replacing $I_{sq}^r(s)$ in (4.36) by ω_r using (4.37):

$$\left[\left(r_s + sL_q + K_p + \frac{K_i}{s}\right) + \frac{\omega_r^2 L_d L_q}{r_s + sL_d + K_p + \frac{K_i}{s}}\right] \frac{\left[s + \left(\frac{P}{2}\right)^2 \frac{D}{J} + \frac{PA}{2J}\right] \omega_r}{\left(\frac{P}{2}\right)^2 \frac{1}{J}\frac{3}{2} \lambda_{sm}'} + \omega_r \lambda_{sm}'^r = \left(K_p + \frac{K_i}{s}\right) I_{sq}^{r*}(s) \tag{4.38}$$

The PMSM model is non-linear due to the presence of ω_r^2 in (4.36) that in turn results in a ω_r^3 factor in (4.38). Thus, it is necessary to linearize the mode before deriving a transfer function between ω_r and I_{sq}^{r*}.

Applying linearization theory, $i_{sq}^r(s)$, ω_r, and $i_{sq}^{r*}(s)$ can each be written as the sum of an operating point and an error as shown here:

$$i_{sq}^{r}(s) = I_{sq}^{r}(s) + \tilde{i}_{sq}^{r}(s) \tag{4.39}$$

$$\omega_r = \Omega_r + \tilde{\omega}_r \tag{4.40}$$

$$i_{sq}^{r*}(s) = I_{sq}^{r*}(s) + \tilde{i}_{sq}^{r*}(s) \tag{4.41}$$

where $I_{sq}^{r}(s)$, Ω_r and $I_{sq}^{r*}(s)$ represent dc operating points, and $\tilde{i}_{sq}^{r}(s)$, $\tilde{\omega}_r$ and $\tilde{i}_{sq}^{r*}(s)$ represent ac small signals.

Equation (4.36) can be rewritten as:

$$\begin{aligned}&\left[\left(r_s + sL_q + K_p + \frac{K_i}{s}\right) + \frac{\left(\Omega_r + \tilde{\omega}_r\right)^2 L_d L_q}{r_s + sL_d + K_p + \frac{K_i}{s}}\right]\left(I_{sq}^{r}(s) + \tilde{i}_{sq}^{r}(s)\right) + \left(\Omega_r + \tilde{\omega}_r\right)\lambda_{sm}'^{r} \\ &= \left(K_p + \frac{K_i}{s}\right)\left(I_{sq}^{r*}(s) + \tilde{i}_{sq}^{r*}(s)\right)\end{aligned} \tag{4.42}$$

Subtracting (4.42) and (4.36) to eliminate operating point variables yields:

$$\left(r_s + sL_q + K_p + \frac{Ki}{s}\right)\tilde{i}_{sq}^{r}(s) + \frac{L_d L_q}{r_s + sL_d + K_p + \frac{K_i}{s}}\left(\Omega_r^2 \tilde{i}_{sq}^{r}(s) + 2\tilde{\omega}_r \Omega_r I_{sq}^{r}(s)\right) + \tilde{\omega}_r \lambda_{sm}'^{r} = \left(K_p + \frac{K_i}{s}\right)\tilde{i}_{sq}^{r*}(s) \tag{4.43}$$

Substitute $\tilde{i}_{sq}^{r}(s)$ and $\tilde{i}_{sq}^{r*}(s)$ in (4.43) by $\tilde{\omega}_r$ through (4.38) and by $\tilde{\omega}_r^*$ through (4.21) seperately:

$$\begin{aligned}&\left\{\left[\left(r_s + sL_q + K_p + \frac{K_i}{s}\right)\left(r_s + sL_d + K_p + \frac{K_i}{s}\right) + L_d L_q \Omega_r^2\right]\frac{s + \left(\frac{P}{2}\right)^2 \frac{D}{J} + \frac{PA}{2J}}{\left(\frac{P}{2}\right)^2 \frac{\lambda_{sm}'}{J}}\frac{2}{3} + 2\Omega_r I_{sq}^{r} L_d L_q + \lambda_{sm}'\left(r_s + sL_d + K_p + \frac{K_i}{s}\right)\right\}\tilde{\omega}_r \\ &= \left(r_s + sL_d + K_p + \frac{K_i}{s}\right)\left(K_p + \frac{K_i}{s}\right)\left(\bar{K}_p + \frac{\bar{K}_i}{s}\right)\left(\tilde{\omega}_r^* - \tilde{\omega}_r\right)\end{aligned}$$

Closed-loop gain of $\tilde{\omega}_r$ over $\tilde{\omega}_r^*$ can be expressed as:

$$\frac{\tilde{\omega}_r}{\tilde{\omega}_r^*} = \frac{n_4 s^4 + n_3 s^3 + n_2 s^2 + n_1 s + n_0}{d_6 s^6 + d_5 s^5 + d_4 s^4 + d_3 s^3 + d_2 s^2 + d_1 s + d_0} \tag{4.44}$$

where

$$n_4 = 3P^2\lambda'_{sm}\bar{K}_p K_p L_d$$

$$n_3 = 3P^2\lambda'_{sm}\left[\bar{K}_i K_p L_d + \bar{K}_p\left(K_p r_s + K_i L_d + K_p^2\right)\right]$$

$$n_2 = 3P^2\lambda'_{sm}\left[\bar{K}_i\left(K_p r_s + K_i L_d + K_p^2\right) + \bar{K}_p\left(2K_p K_i + K_i r_s\right)\right]$$

$$n_1 = 3P^2\lambda'_{sm}\left[\bar{K}_p K_i^2 + \bar{K}_i\left(2K_p K_i + K_i r_s\right)\right]$$

$$n_0 = 3P^2\lambda'_{sm}\bar{K}_i K_i^2$$

$$d_6 = 8JL_d L_q$$

$$d_5 = \left(2DP^2 + 4PA\right)L_d L_q + 8J\left(L_d r_s + L_q r_s + K_p L_q + K_p L_d\right)$$

$$d_4 = 3P^2\lambda'_{sm}\left(\lambda''_{sm}L_d + \bar{K}_p K_p L_d\right) + \left(2DP^2 + 4PA\right)\left(L_d r_s + L_q r_s + K_p L_q + K_p L_d\right) + 8J\left(\Omega_r^2 L_d L_q + r_s^2 + 2K_p r_s + K_i L_q + K_p^2 + K_i L_d\right)$$

$$d_3 = 6P^2\lambda'_{sm}\Omega_r L_d L_q I^r_{sq} + 3P^2\lambda'_{sm}\left[\bar{K}_i K_p L_d + \lambda''_{sm}\left(K_p + r_s\right) + \bar{K}_p\left(K_p r_s + K_i L_d + K_p^2\right)\right] + \left(2DP^2 + 4PA\right)\left(\Omega_r L_d L_q + r_s^2 + 2K_p r_s + K_i L_q + K_p^2 + K_i L_d\right) + 16J\left(K_i r_s + K_p K_i\right)$$

$$d_2 = 3P^2\lambda'_{sm}\left[\lambda''_{sm}K_i + \bar{K}_i\left(K_p r_s + K_i L_d + K_p^2\right) + \bar{K}_p\left(2K_p K_i + K_i r_s\right)\right] + 8JK_i^2 + \left(4DP^2 + 8PA\right)\left(K_i r_s + K_p K_i\right)$$

$$d_1 = \left(2DP^2 + 4PA\right)K_i^2 + 3P^2\lambda'_{sm}\left[\bar{K}_p K_i^2 + \bar{K}_i\left(2K_p K_i + K_i r_s\right)\right]$$

$$d_0 = 3P^2\lambda'_{sm}\bar{K}_i K_i^2$$

4.2.1.2 Synchronous Reference Frame PI Control with Actual Current EMF Compensation

As with the actual-current EMF compensation analyzed in Chapter 3, EMF compensation here is added to the output of the PI controller. However, since the flux linkage equations for the

PMSM differ from those of the RL circuit due to the rotor permanent magnets, the expression for the EMF compensation here is different.

The voltage-current equation of the synchronous reference PI controller with EMF compensation in the *s* domain is:

$$V_{sd}^{r}(s)=\left(K_p+\frac{K_i}{s}\right)\left(I_{sd}^{r*}(s)-I_{sd}^{r}(s)\right)-\hat{\omega}_r\hat{L}_q I_{sq}^{r}(s) \tag{4.45}$$

$$V_{sq}^{r}(s)=\left(K_p+\frac{K_i}{s}\right)\left(I_{sq}^{r*}(s)-I_{sq}^{r}(s)\right)+\hat{\omega}_r L_d I_{sd}^{r}(s)+\hat{\omega}_r\lambda_{sm}^{\prime r} \tag{4.46}$$

Equating (4.32) and (4.33) with (4.45) and (4.46) respectively yields:

$$\left(r_s+sL_d+K_p+\frac{K_i}{s}\right)I_{sd}^{r}(s)=\left(\omega_r L_q-\hat{\omega}_r\hat{L}_q\right)I_{sq}^{r}(s) \tag{4.47}$$

$$\begin{aligned}&\left(r_s+s\hat{L}_q+K_p+\frac{K_i}{s}\right)I_{sq}^{r}(s)+\left(\omega_r L_d-\hat{\omega}_r L_d\right)I_{sd}^{r}(s)+\left(\omega_r-\hat{\omega}_r\right)\lambda_{sm}^{\prime r}\\&=\left(K_p+\frac{K_i}{s}\right)I_{sq}^{r*}(s)\end{aligned} \tag{4.48}$$

Combining (4.47) and (4.48):

$$\begin{aligned}&\left[\left(r_s+s\hat{L}_q+K_p+\frac{K_i}{s}\right)+\frac{\left(\omega_r L_d-\hat{\omega}_r L_d\right)\left(\omega_r L_q-\hat{\omega}_r\hat{L}_q\right)}{\left(r_s+sL_d+K_p+\frac{K_i}{s}\right)}\right]I_{sq}^{r}(s)+\left(\omega_r-\hat{\omega}_r\right)\lambda_{sm}^{\prime r}\\&=\left(K_p+\frac{K_i}{s}\right)I_{sq}^{r*}(s)\end{aligned} \tag{4.49}$$

Applying the linearization method used previously yields:

$$\begin{aligned}&\left(r_s+s\hat{L}_q+K_p+\frac{Ki}{s}\right)\tilde{i}_{sq}^{r}(s)+\frac{L_d\hat{L}_q}{r_s+sL_d+K_p+\frac{K_i}{s}}\left[\left(\Omega_r-\hat{\Omega}_r\right)^2\tilde{i}_{sq}^{r}(s)+2\tilde{\omega}_r\left(\Omega_r-\hat{\Omega}_r\right)I_{sq}^{r}(s)\right]+\tilde{\omega}_r\lambda_{sm}^{\prime r}\\&=\left(K_p+\frac{K_i}{s}\right)\tilde{i}_{sq}^{r*}(s)\end{aligned}$$

(4.50)

Comparing (4.50) to (4.43), the only difference is that Ω_r has been replaced by $\left(\Omega_r - \hat{\Omega}_r\right)$ where $\hat{\Omega}_r$ represents the estimated steady state rotor velocity – we are neglecting any small signal component of the estimated rotor velocity. Consequently, the transfer function does not need to be re-derived step by step; instead replacing Ω_r in (4.44) by $\left(\Omega_r - \hat{\Omega}_r\right)$ yields:

$$\frac{\tilde{\omega}_r}{\tilde{\omega}_r^*} = \frac{n_4 s^4 + n_3 s^3 + n_2 s^2 + n_1 s + n_0}{d_6 s^6 + d_5 s^5 + d_4 s^4 + d_3 s^3 + d_2 s^2 + d_1 s + d_0} \tag{4.51}$$

where

$$n_4 = 3P^2 \lambda'_{sm} \bar{K}_p K_p L_d$$

$$n_3 = 3P^2 \lambda'_{sm} \left[\bar{K}_i K_p L_d + \bar{K}_p \left(K_p r_s + K_i L_d + K_p^2 \right) \right]$$

$$n_2 = 3P^2 \lambda'_{sm} \left[\bar{K}_i \left(K_p r_s + K_i L_d + K_p^2 \right) + \bar{K}_p \left(2K_p K_i + K_i r_s \right) \right]$$

$$n_1 = 3P^2 \lambda'_{sm} \left[\bar{K}_p K_i^2 + \bar{K}_i \left(2K_p K_i + K_i r_s \right) \right]$$

$$n_0 = 3P^2 \lambda'_{sm} \bar{K}_i K_i^2$$

$$d_6 = 8JL_d L_q$$

$$d_5 = \left(2DP^2 + 4PA \right) L_d L_q + 8J \left(L_d r_s + L_q r_s + K_p L_q + K_p L_d \right)$$

$$d_4 = 3P^2 \lambda'_{sm} \left(\lambda'^r_{sm} L_d + \bar{K}_p K_p L_d \right) + \left(2DP^2 + 4PA \right) \left(L_d r_s + L_q r_s + K_p L_q + K_p L_d \right) + 8J \left[\left(\Omega_r - \hat{\Omega}_r \right)^2 L_d L_q + r_s^2 + 2K_p r_s + K_i L_q + K_p^2 + K_i L_d \right]$$

$$d_3 = 6P^2 \lambda'_{sm} \left(\Omega_r - \hat{\Omega}_r \right) L_d L_q I^r_{sq} + 3P^2 \lambda'_{sm} \left[\lambda'^r_{sm} \left(K_p + r_s \right) + \bar{K}_i K_p L_d + \bar{K}_p \left(K_p r_s + K_i L_d + K_p^2 \right) \right] + \left(2DP^2 + 4PA \right) \left[\left(\Omega_r - \hat{\Omega}_r \right)^2 L_d L_q + r_s^2 + 2K_p r_s + K_i L_q + K_p^2 + K_i L_d \right] + 16J \left(K_i r_s + K_p K_i \right)$$

$$d_2 = 3P^2\lambda'_{sm}\left[\lambda''_{sm}K_i + \bar{K}_i\left(K_p r_s + K_i L_d + K_p^2\right) + \bar{K}_p\left(2K_p K_i + K_i r_s\right)\right] + 8JK_i^2 + \left(4DP^2 + 8PA\right)\left(K_i r_s + K_p K_i\right)$$

$$d_1 = \left(2DP^2 + 4PA\right)K_i^2 + 3P^2\lambda'_{sm}\left[\bar{K}_p K_i^2 + \bar{K}_i\left(2K_p K_i + K_i r_s\right)\right]$$

$$d_0 = 3P^2\lambda'_{sm}\bar{K}_i K_i^2$$

4.2.1.3 Synchronous Reference Frame PI Control with Reference Current EMF Compensation

The voltage-current equations of the synchronous reference frame PI control with the reference current EMF compensation are:

$$V_{sd}^r(s) = \left(K_p + \frac{K_i}{s}\right)\left(I_{sd}^{r*}(s) - I_{sd}^r(s)\right) - \hat{\omega}_r\hat{L}_q I_{sq}^{r*}(s) \tag{4.52}$$

$$V_{sq}^r(s) = \left(K_p + \frac{K_i}{s}\right)\left(I_{sq}^{r*}(s) - I_{sq}^r(s)\right) + \hat{\omega}_r L_d I_{sd}^{r*}(s) + \hat{\omega}_r\lambda''_{sm} \tag{4.53}$$

Equating (4.32) and (4.33) with (4.52) and (4.53) respectively yields:

$$\left(r_s + sL_d + K_p + \frac{K_i}{s}\right)I_{sd}^r(s) = \omega_r\hat{L}_q I_{sq}^r(s) - \hat{\omega}_r\hat{L}_q I_{sq}^{r*}(s) \tag{4.54}$$

$$\left(r_s + s\hat{L}_q + K_p + \frac{K_i}{s}\right)I_{sq}^r(s) + \omega_r L_d I_{sd}^r(s) + \left(\omega_r - \hat{\omega}_r\right)\lambda''_{sm} = \left(K_p + \frac{K_i}{s}\right)I_{sq}^{r*}(s) \tag{4.55}$$

Combining (4.54) and (4.55):

$$\left(r_s + s\hat{L}_q + K_p + \frac{K_i}{s}\right)I_{sq}^r(s) + \frac{\omega_r L_d}{r_s + sL_d + K_p + \frac{K_i}{s}}\left(\omega_r L_d I_{sq}^r(s) - \hat{\omega}_r\hat{L}_q I_{sq}^{r*}(s)\right) + \left(\omega_r - \hat{\omega}_r\right)\lambda''_{sm} = \left(K_p + \frac{K_i}{s}\right)I_{sq}^{r*}(s) \tag{4.56}$$

Applying the linearization method used before, the small signal equation is:

$$\begin{aligned}&\left(r_s+sL_q+K_p+\frac{K_i}{s}\right)\tilde{i}_{sq}^{r}+\frac{L_d^2\left(\Omega_r^2\tilde{i}_{sq}^{r}+2\Omega_r\hat{\Omega}_r I_{sq}^{r}\right)}{r_s+sL_d+K_p+\frac{K_i}{s}}+\hat{\Omega}_r\lambda_{sm}'^{r}\\&=\left(K_p+\frac{K_i}{s}\right)\tilde{i}_{sq}^{r*}+\frac{\hat{\Omega}_r L_d L_q}{r_s+sL_d+K_p+\frac{K_i}{s}}\left(\hat{\Omega}_r I_{sq}^{r*}+\Omega_r\tilde{i}_{sq}^{r*}\right)\end{aligned}\tag{4.57}$$

Close-loop gain is:

$$\frac{\tilde{\omega}_r}{\tilde{\omega}_r^*}=\frac{n_4s^4+n_3s^3+n_2s^2+n_1s+n_0}{d_6s^6+d_5s^5+d_4s^4+d_3s^3+d_2s^2+d_1s+d_0}\tag{4.58}$$

where

$$n_4=3P^2\lambda_{sm}'\bar{K}_pK_pL_d$$

$$n_3=3P^2\lambda_{sm}'\left[\tilde{K}_iK_pL_d+\bar{K}_p\left(K_pr_s+K_iL_d+K_p^2+2\hat{\Omega}_r\Omega_rL_dL_q\right)\right]$$

$$n_2=3P^2\lambda_{sm}'\left[\bar{K}_i\left(K_pr_s+K_iL_d+K_p^2+2\hat{\Omega}_r\Omega_rL_dL_q\right)+\bar{K}_p\left(2K_pK_i+K_ir_s\right)\right]$$

$$n_1=3P^2\lambda_{sm}'\left[\bar{K}_pK_i^2+\bar{K}_i\left(2K_pK_i+K_ir_s\right)\right]$$

$$n_0=3P^2\lambda_{sm}'\bar{K}_iK_i^2$$

$$d_6=8JL_dL_q$$

$$d_5=\left(2DP^2+4PA\right)L_dL_q+8J\left(r_sL_q+r_sL_d+K_pL_q+K_pL_d\right)$$

$$\begin{aligned}d_4=&\left(2DP^2+4PA\right)\left(r_sL_q+r_sL_d+K_pL_q+K_pL_d\right)\\&+8J\left(r_s^2+2K_pr_s+K_iL_d+K_iL_q+K_p^2\right)+3P^2\lambda_{sm}'L_d\left(\lambda_{sm}'^{r}+\bar{K}_pK_p\right)\end{aligned}$$

$$\begin{aligned}d_3=3P^2\lambda_{sm}'\Big[&2\Omega_rI_{sq}^{r}L_d^2+\bar{K}_iK_pL_d-\hat{\Omega}_rI_{sq}^{r*}L_dL_q+\lambda_{sm}'^{r}\left(K_p+r_s\right)\\&+\bar{K}_p\left(K_pr_s+K_iL_d+K_p^2+2\hat{\Omega}_r\Omega_rL_dL_q\right)\Big]\\&+\left(2DP^2+4PA\right)\left(r_s^2+2K_pr_s+K_iL_q+K_p^2+K_iL_d\right)+16J\left(K_ir_s+K_pK_i\right)\end{aligned}$$

$$d_2 = 3P^2\lambda'_{sm}\left[\lambda''^{r}_{sm}K_i + \bar{K}_i\left(K_p r_s + K_i L_d + K_p^2 + 2\hat{\Omega}_r\Omega_r L_d L_q\right) + \bar{K}_p\left(2K_pK_i + K_i r_s\right)\right]$$
$$+8JK_i^2 + \left(4DP^2 + 8PA\right)\left(K_i r_s + K_p K_i\right)$$

$$d_1 = \left(2DP^2 + 4PA\right)K_i^2 + 3P^2\lambda'_{sm}\left[\bar{K}_i\left(2K_pK_i + K_i r_s\right) + \bar{K}_p K_i^2\right]$$

$$d_0 = 3P^2\lambda'_{sm}\bar{K}_i K_i^2$$

To verify the derivation of (4.51), its step response is compared to the ratio of the actual velocity over reference velocity from a time-domain simulation in Figure 4-3.

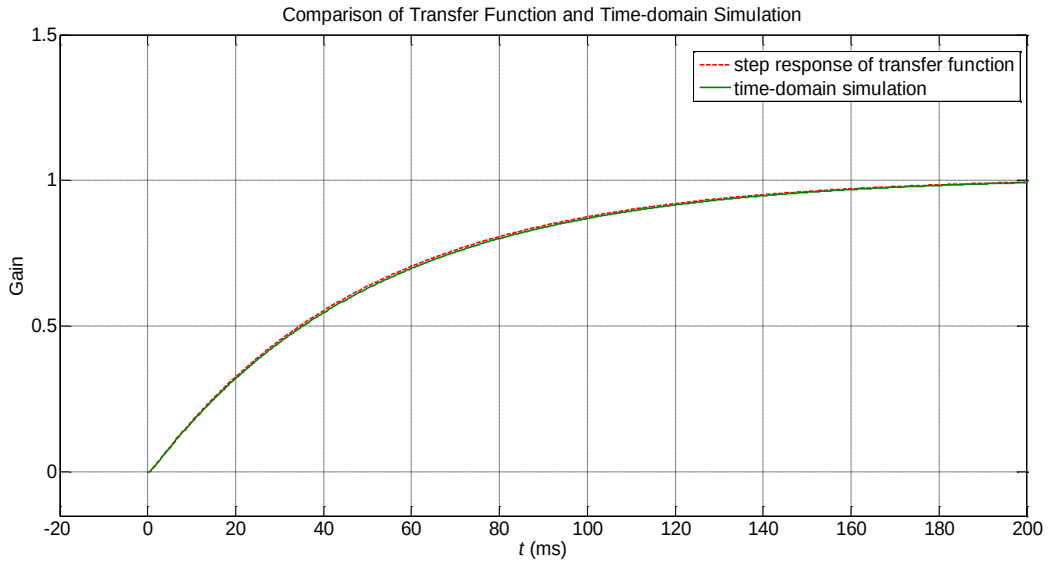

Figure 4-3. Comparison of transfer function and time-domain simulation.

4.2.2 Transfer Function Analysis

Inspecting (4.44), (4.51) and (4.58) reveals that the expressions for the closed-loop gain between reference velocity and feedback velocity of the PMSM are different when using synchronous reference frame PI controller, synchronous reference frame PI controller with actual current EMF compensation, and synchronous reference frame PI controller with reference current EMF. However, after substituting all parameter values from Table 2-1 into these equations, there

are only a few small differences in the transfer function coefficient values. Because synchronous reference frame with actual current emf compensation is the most common as discussed in Chapter 3, only that method will be analyzed further.

Root-locus of closed-loop gain of synchronous reference frame with actual current emf compensation is shown in Figure 4-4. Since all roots are located in the left half plane, the system remains stable. However, similar to the current regulation discussed in Chapter 3, there still exists bandwidth limitation, which would affect response time.

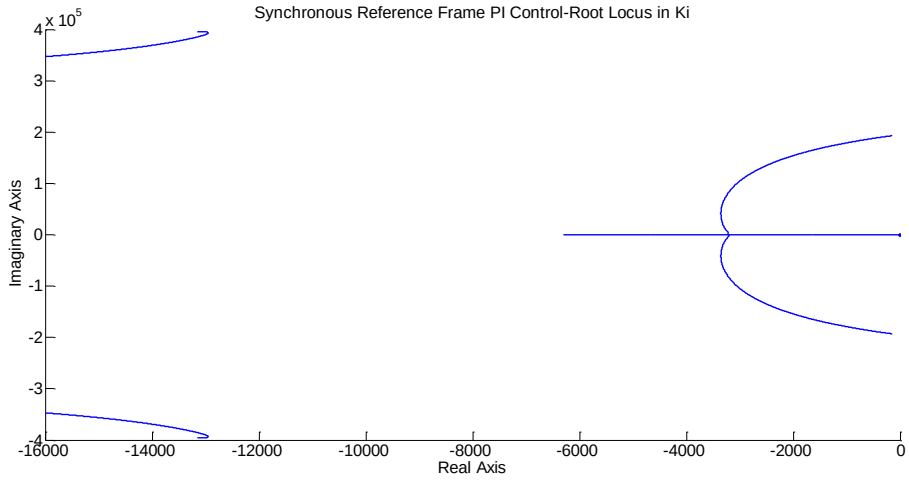

Figure 4-4. Root-locus for K_i of synchronous reference frame PI control.

4.3 Comparison

Since by using synchronous reference frame PI control, there still exists bandwidth limitation in velocity control of PMSM. Response time of two reference frames would be different. Step responses of these two are shown in Figure 4-5. From the figure, stationary reference frame proportional control yields a faster response time.

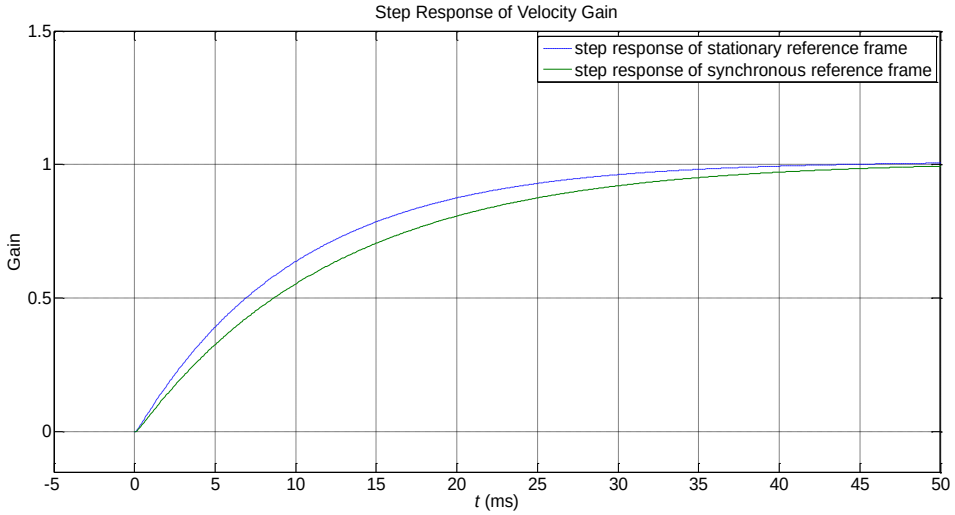

Figure 4-5. Comparison of step for stationary and synchronous reference frame control.

Simulations of the PMSM drive system are shown in Figures 4-6 and 4-7 while velocity comparison is shown in Figure 4-8:

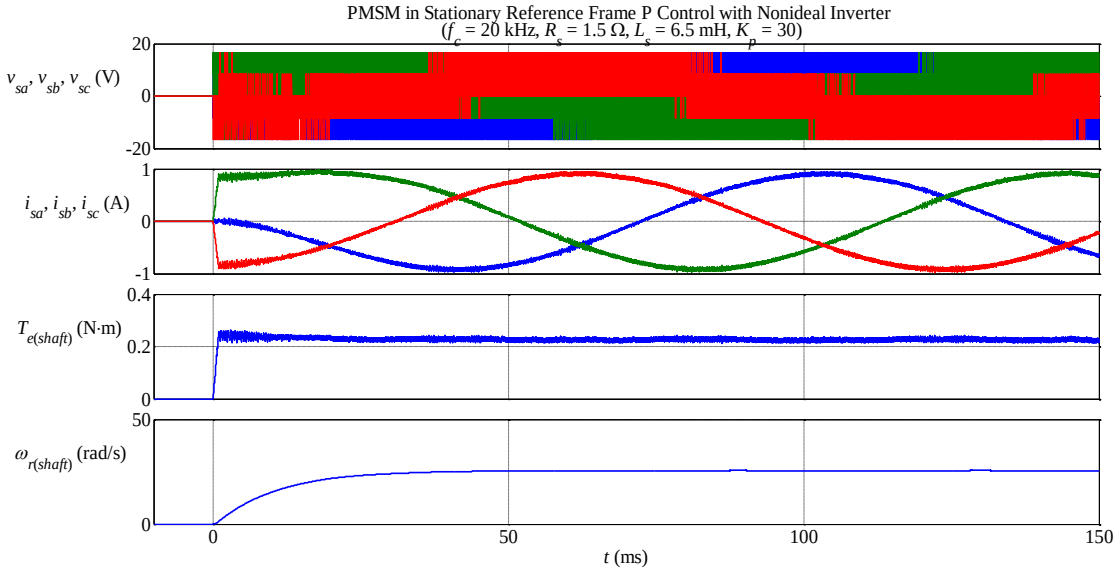

Figure 4-6. Simulation result of PMSM in stationary reference frame proportional control.

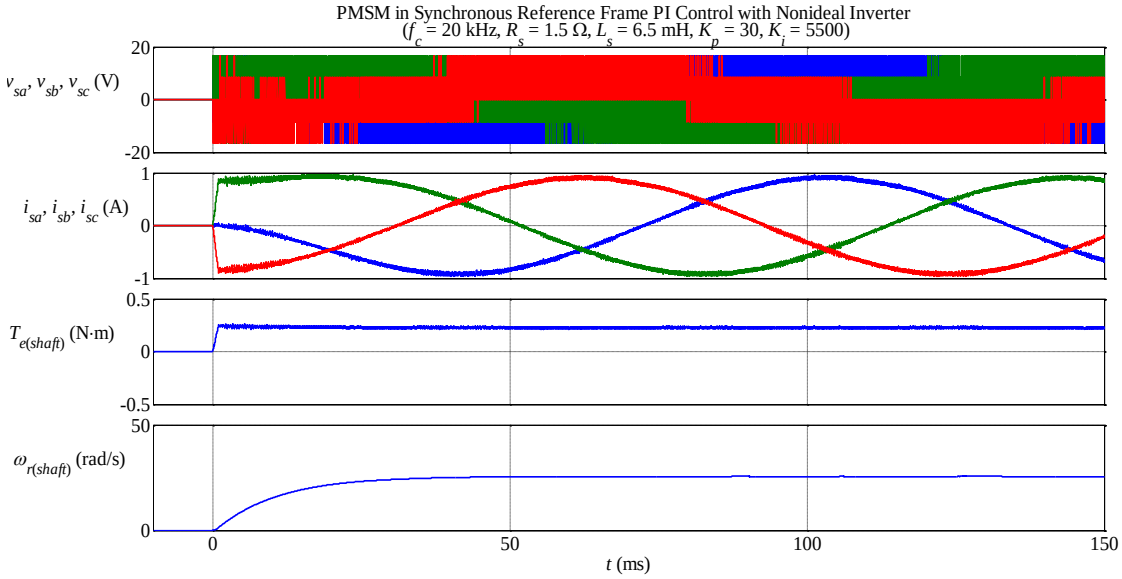

Figure 4-7. Simulation result of PMSM in synchronous reference frame PI control with actual current emf compensation.

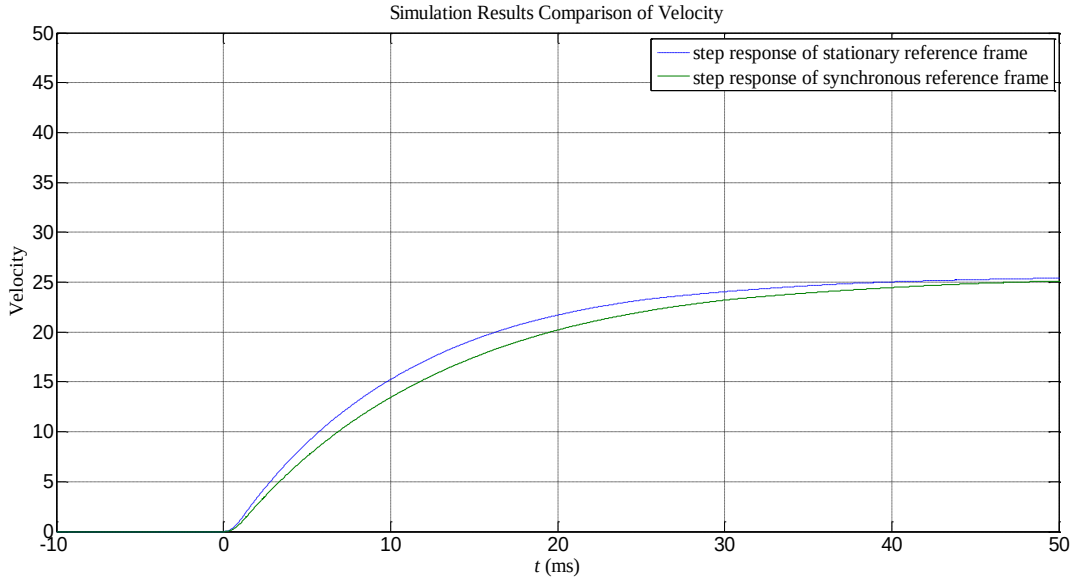

Figure 4-8. Velocity comparison of Simulation result between stationary and synchronous reference frame control.

Chapter 5

Conclusion

Much of the research literature and commercial development related to field-oriented control in permanent magnet synchronous machines has utilized synchronous reference frame PI control for the inner current loop, as this method avoids controller hardware bandwidth limitation by converting ac quantities to dc quantities in the steady state (lower frequency ac quantities in the transient). With the availability of faster controller hardware, however, the transformation to low frequency signals is not necessary. Moreover, the combination of the transformation and PI control results in a bandwidth limit for the control algorithm itself. This limit has been examined in this thesis for an RL circuit by deriving an expression for the closed-loop gain and simulating the transient response.

Stationary reference frame proportional control has been proposed as an alternative. This method has also been examined in this thesis for an RL circuit using the same techniques. This work has confirmed the higher bandwidth limit for the stationary reference frame proportional control in an RL circuit.

The results for an RL circuit have also been extended to a complete PMSM drive system. Due to the nonlinear nature of the PMSM, the very first step is to linearize PMSM mathematical equation, and bandwidth limitation similar to RL circuit is then analyzed and demonstrated by Simulink. This bandwidth limitation would cause the increase of response time which is not good for the system performance.

In the future, synchronous reference frame proportional control could be considered to see if there exists bandwidth limitation, and compared with stationary reference frame proportional control to check its performance in PMSM drive system.

References

[1] P. Pillay and R. Krishnan, "Application Characteristics of Permanent Magnet Synchronous and Brushless dc Motors for Servo Drives", IEEE Transactions on Industry Applications, Vol. 27, No. 5, September/October 1991.

[2] R. Yu, H. Zhang, G. Tan, and D. Yan, "Design of Robust Controller for PMSM Drivers", 2010 International Conference on Electrical and Control Engineering.

[3] M. Rahimi, M. Momeni, and K. Abbaszadeh, "A New Approach to Minimize Torque Pulsations in PMSM Driven by Field Oriented Control", International Symposium on Power Electronics, Electrical Drives, Automation and Motion, 2010.

[4] J. Park, C. Khalizadeh, and H. Hofmann, "Design ad Control of High-speed Solid-rotor Synchronous Reluctance Drive with Three-phase LC Filter", in 39th IEEE Industry Application Society Annual Meeting Record. ISBN 0-7803-9208-6.

[5] M. P. Kazmierkowski, "Current Control Techniques for Three-Phase Voltage-Source PWM Converters: A Survey", IEEE Transactions on Industrial Electronics, Vol. 45, No. 5, October 1998.

[6] O. Elgerd, "Electric Energy Systems Theory: An Introduction", Tata McGraw-Hill. pp. 35–39. ISBN 978-0070192300.

[7] P. K. Sadhu, G. Sarkar, and A. Rakshit, "A microcontroller-based variable voltage variable frequency sinusoidal power source with a novel PWM generation strategy", Measurement, 2012 – Elsevier, Volume 45, Issue 1, January 2012, Pages 59–67. (Article)

[8] B. Ismail, "Development of a Single Phase SPWM Microcontroller-Based Inverter", First International Power and Energy Conference PEC, 2006

[9] I. Colak and E. Kabalci, "Developing a novel sinusoidal pulse width modulation (SPWM) technique to eliminate side band harmonics", International Journal of Electrical Power & Energy System, Volume 44, Issue 1, January 2013 – Elsevier, Pages 861–871. (Article)

[10] N. Raju, M. Islam, and A. Uddin, “Sinusoidal PWM Signal Generation Technique for Three Phase Voltage Source Inverter with Analog Circuit & Simulation of PWM Inverter for Standalone Load & Micro-grid System”, International Journal of Renewable Energy, Vol.3, No.3.

[11] L. You, Z. Ma, X. Wang, and H. Zhang, “Sliding Mode Control For Permanent Magnet Synchronous Motor Based On A Double Closed-loop Decoupling Method”, Fourth International Conference on Machine Learning and Cybernetics, Guangzhou, 18-21 August 2005.

Appendix

Simulink Block Diagram of PMSM Drive System

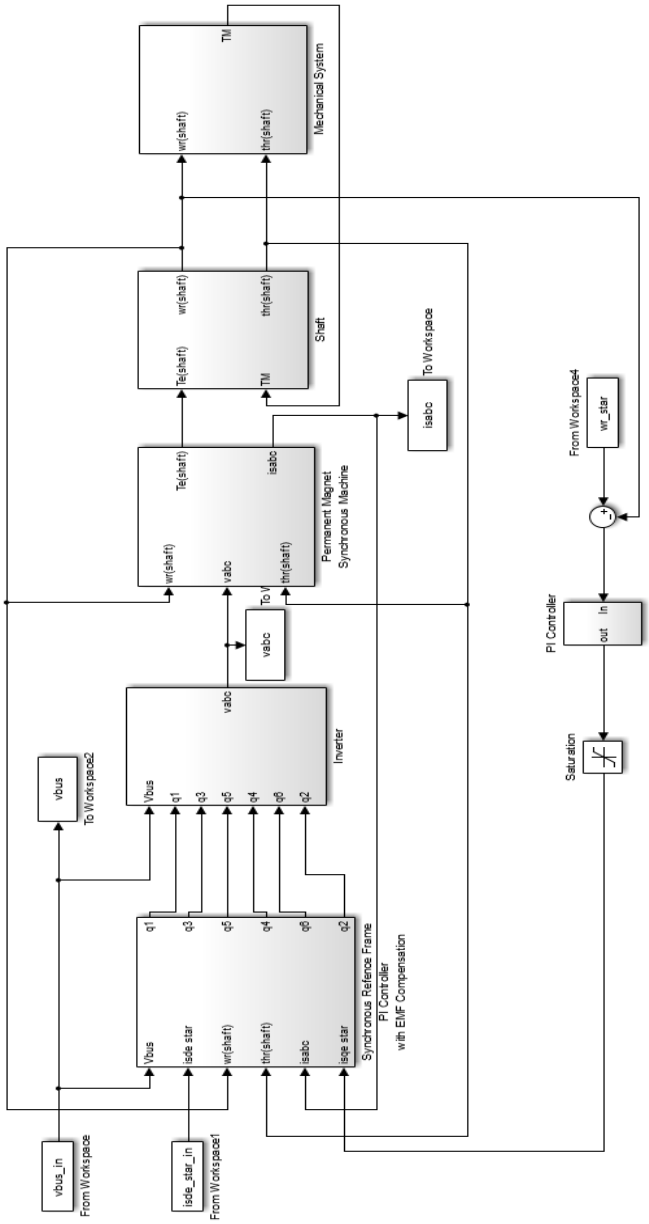

Figure A-1 PMSM Drive System

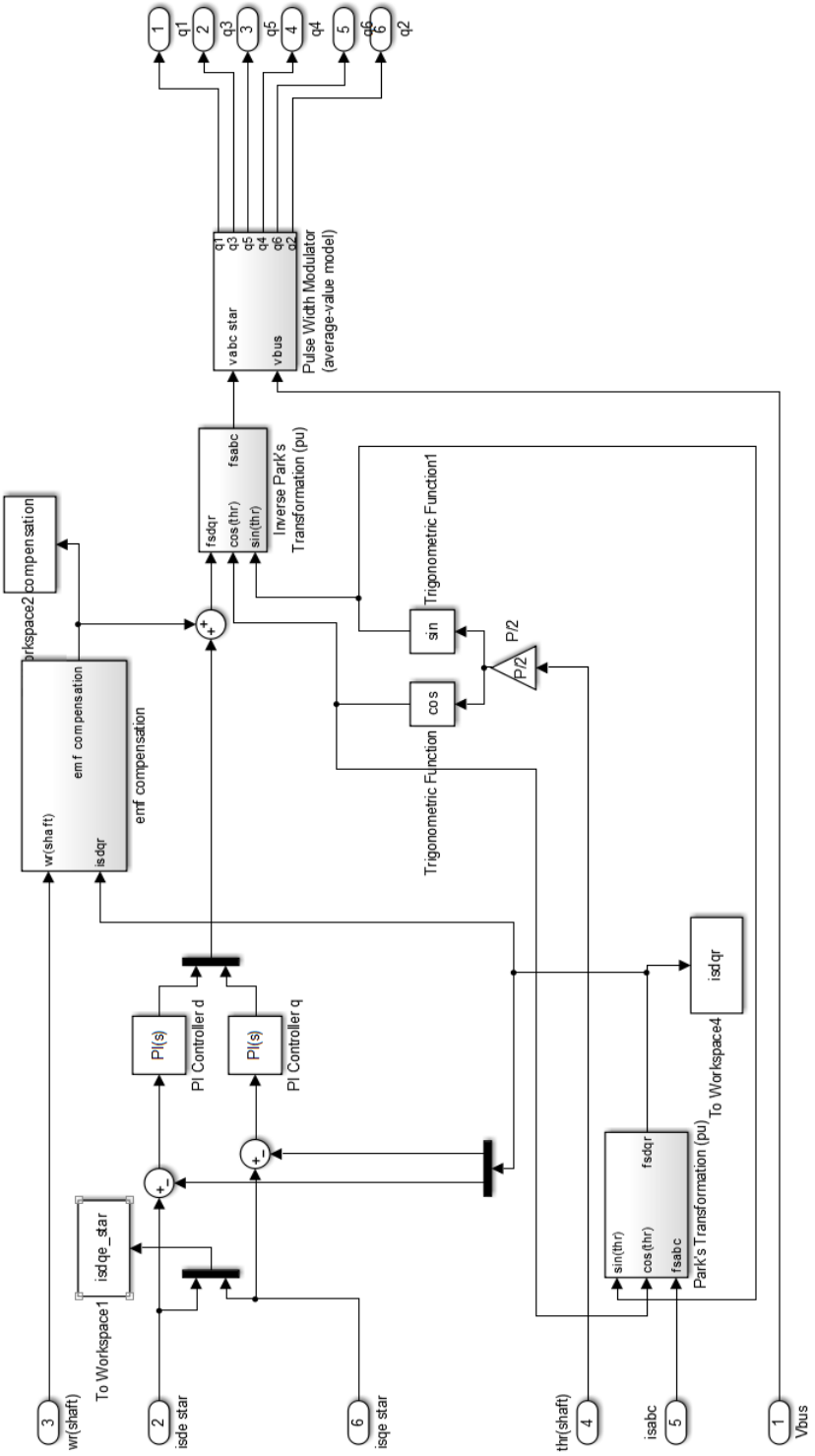

Figure A-2 Synchronous Reference Frame PI Controller with EMF Compensation

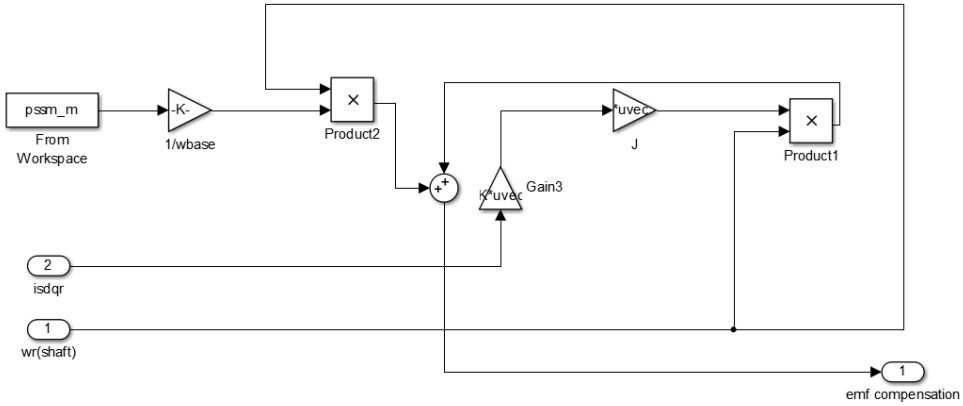

Figure A-3 Emf Compensation

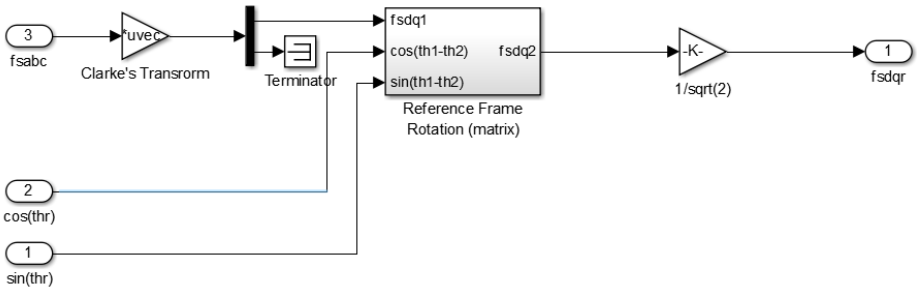

Figure A-4 Park's Transform

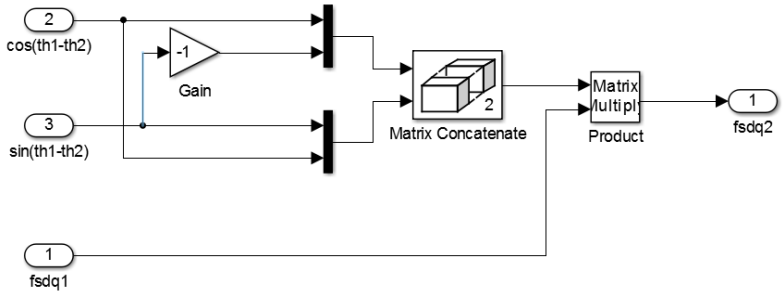

Figure A-5 Reference Frame Rotation (matrix)

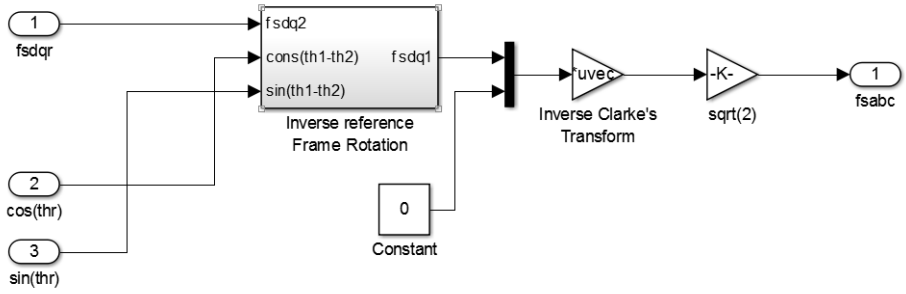

Figure A-6 Inverse Park's Transform

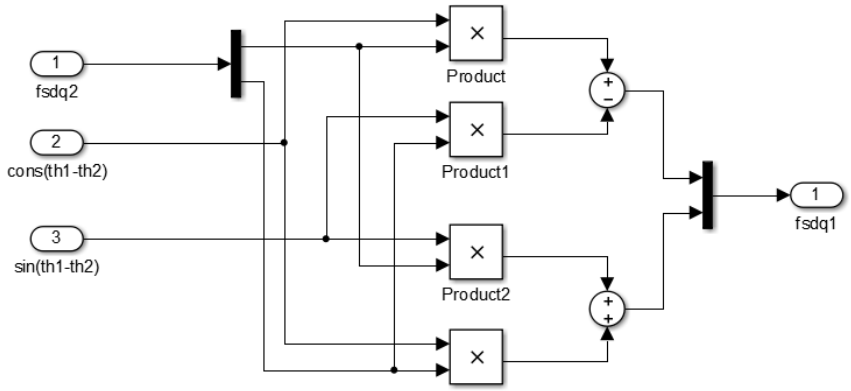

Figure A-7 Inverse reference Frame Rotation

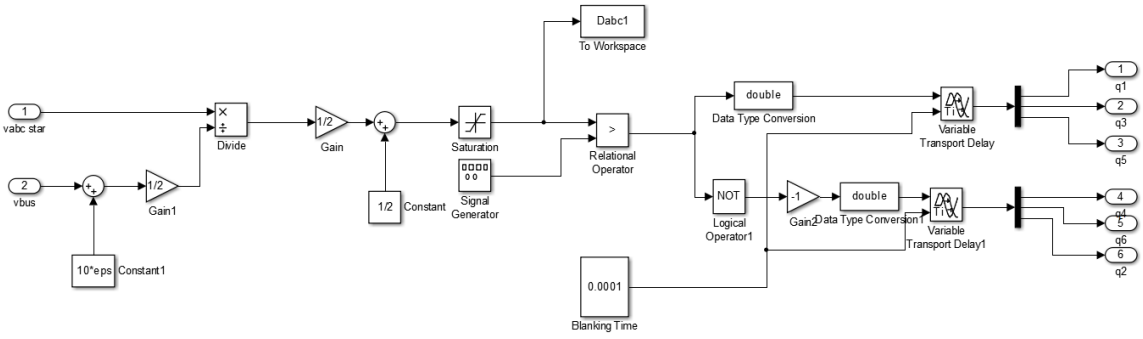

Figure A-8 Pulse Width Modulator

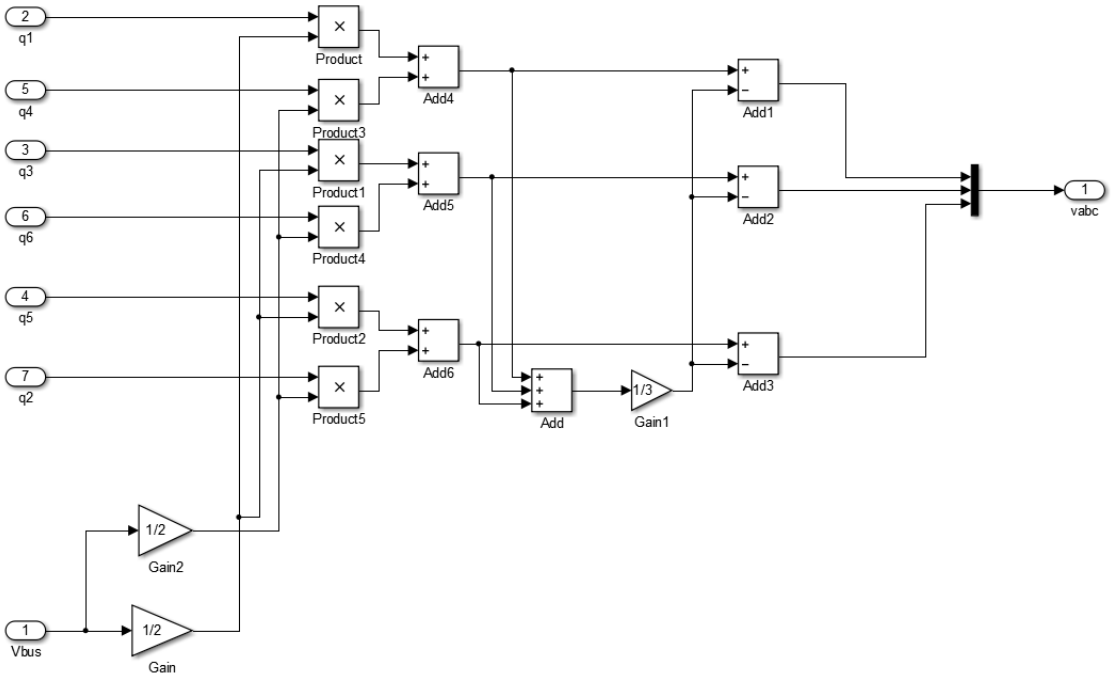

Figure A-9 Inverter

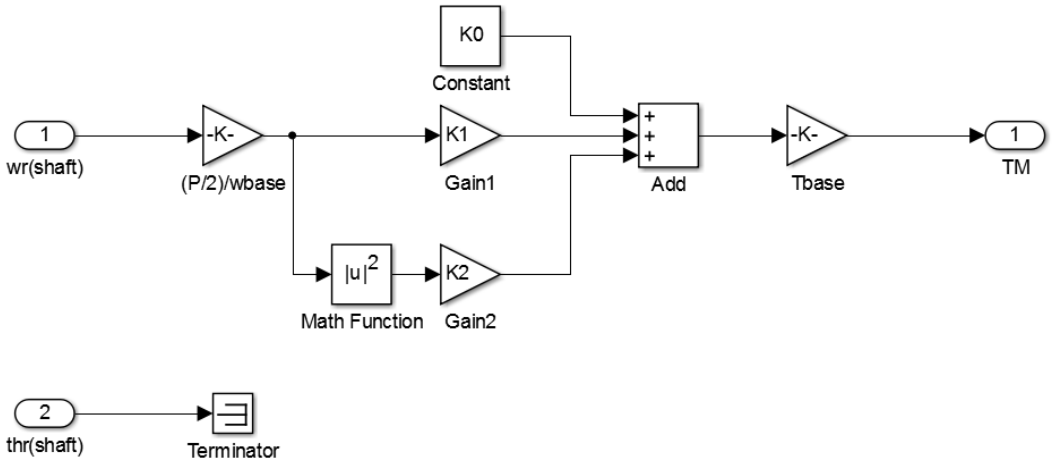

Figure A-10 Mechanical System

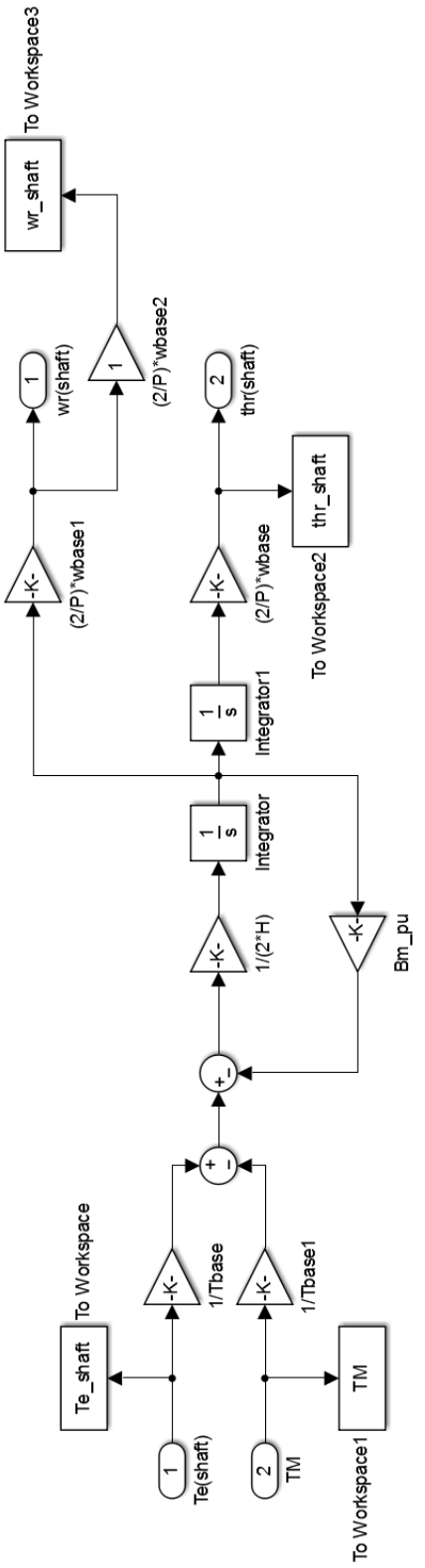

Figure A-11 Shaft

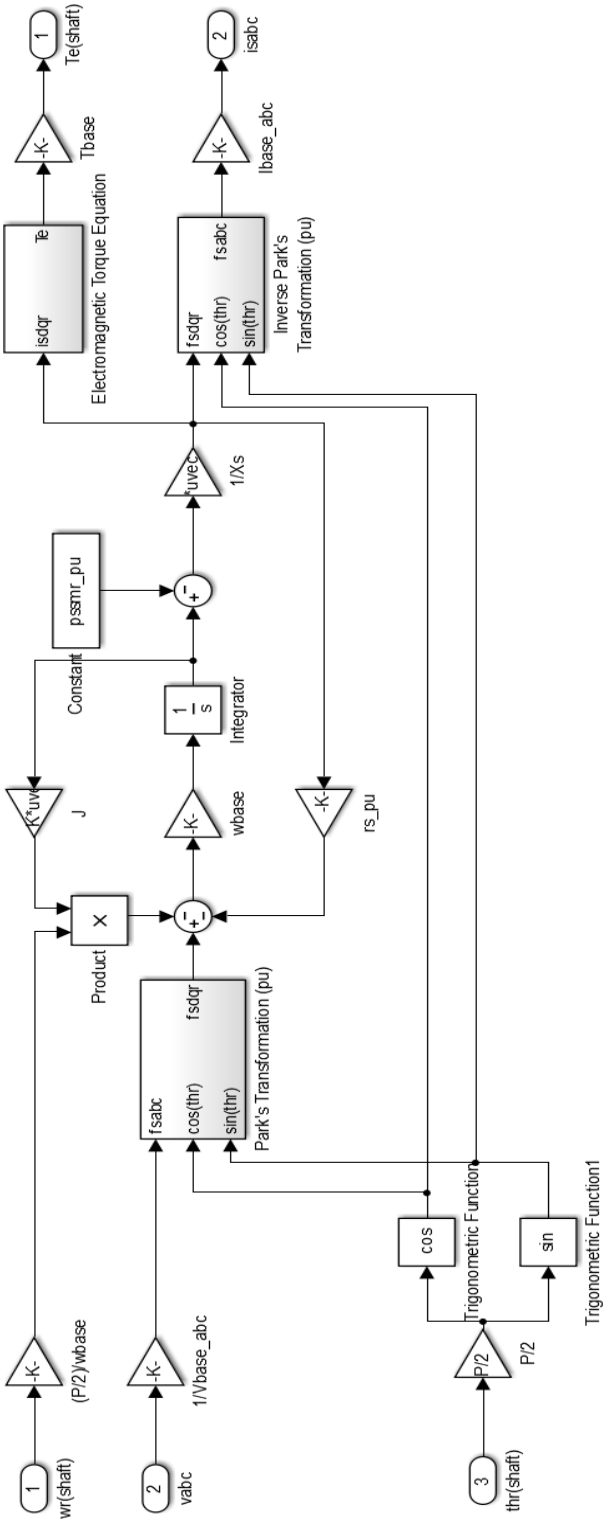

Figure A-12 PMSM

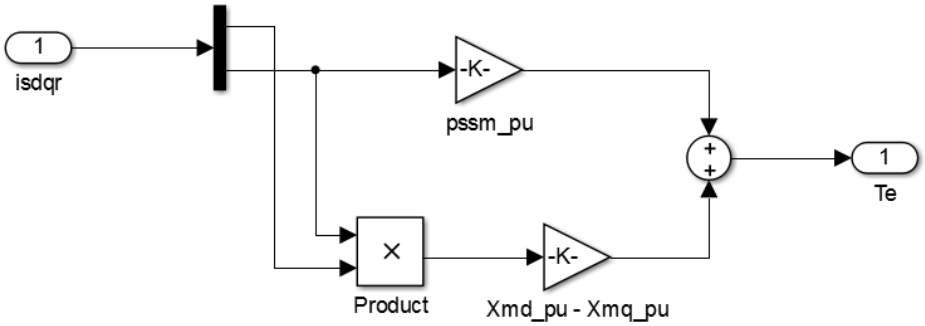

Figure A-13 Electromagnetic Torque Equation

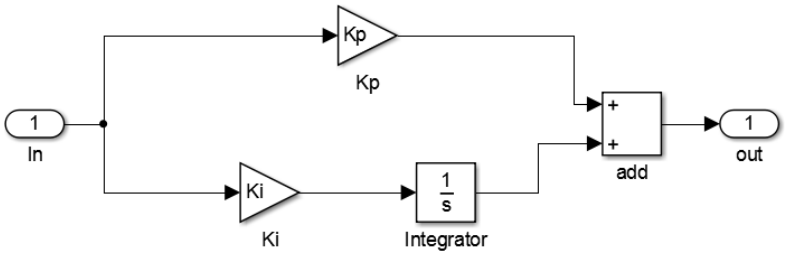

Figure A-14 Velocity PI Controller